# Anisamide-Anchored Lyotropic Nano-Liquid Crystalline Particles with AIE Effect: A Smart Optical Beacon for Tumor Imaging and Therapy

Sandeep Urandur,[†] Venkatesh Teja Banala,[†] Ravi Prakash Shukla,[†] Naresh Mittapelly,[†] Gitu Pandey,[†] Navodayam Kalleti,[‡] Kalyan Mitra,[§] Srikanta Kumar Rath,[‡] Ritu Trivedi,[||] Pratibha Ramarao,[⊥] and Prabhat Ranjan Mishra*,[†]

[†]Division of Pharmaceutics, [‡]Division of Toxicology, [§]Electron Microscopy Division, and [||]Division of Endocrinology, CSIR-Central Drug Research Institute, Lucknow 226031, India
[⊥]Soft Condensed Matter Lab, Raman Research Institute, Bangalore 560080, India

**S** Supporting Information

**ABSTRACT:** The prospective design of nanocarriers for personalized oncotherapy should be an ensemble of targeting, imaging, and noninvasive therapeutic capabilities. Herein, we report the development of the inverse hexagonal nano-liquid crystalline (NLC) particles that are able to host formononetin (FMN), a phytoestrogen with known anticancer activity, and tetraphenylethene (TPE), an iconic optical beacon with aggregation-induced emission (AIE) signature, simultaneously. Ordered three-dimensional mesoporous internal structure and high-lipid-volume fraction of NLC nanoparticles (NLC NPs) frame the outer compartment for the better settlement of payloads. Embellishment of these nanoparticles by anisamide (AA), a novel sigma receptor targeting ligand using carbodiimide coupling chemistry ensured NLC's as an outstanding vehicle for possible utility in surveillance of tumor location as well as the FMN delivery through active AIE imaging. The size and structural integrity of nanoparticles were evaluated by quasi-elastic light scattering, cryo field emission scanning electron microscopy small-angle X-ray scattering. The existence of AIE effect in the nanoparticles was evidenced through the photophysical studies that advocate the application of NLC NPs in fluorescence-based bioimaging. Moreover, confocal microscopy illustrated the single living cell imaging ability endowed by the NLC NPs. In vitro and in vivo studies supported the enhanced efficacy of targeted nanoparticles (AA-NLC-TF) in comparison to nontargeted nanoparticles (NLC-TF) and free drug. Apparently, this critically designed multimodal NLC NPs may establish a promising platform for targeted and image-guided chemotherapy for breast cancer.

**KEYWORDS:** liquid crystals, formononetin, aggregation-induced emission, optical imaging, sigma receptors
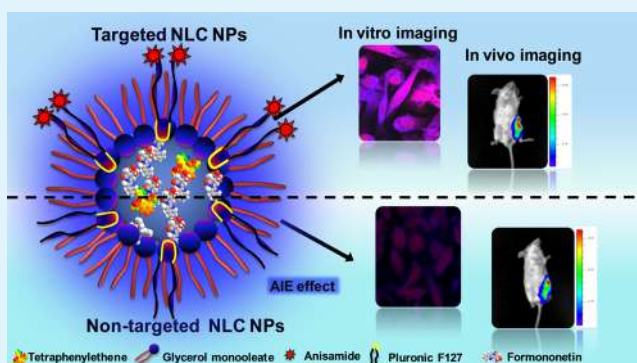
## 1. INTRODUCTION

The development of multifunctional nanoparticles for synchronized imaging and tumor-targeted noninvasive therapy through optical imaging is supposed to have a notable impact on future personalized oncology. Routine X-ray mammography to detect breast cancer involves exposure to harmful ionizing radiation and experiences poor diagnostic accuracy, resulting in a high rate of false-positive diagnosis.[1−3] In contrast, emerging optical fluorescence imaging modality is safe, inexpensive, accurate, and detect cancer at a primitive stage long before the phenotypic changes occur with excellent spatial resolution.[4] Among various contrast agents employed for bioimaging, optical beacons with distinct aggregation-induced emission (AIE) property has been gaining importance nowadays and outperforms the flaws of inorganic contrast agents like small Stokes shift, low photostability, low molar absorptivity and

heavy metal cytotoxicity.[5,6] Thus, AIE fluorogens opened a new avenue in the development of stable and cytocompatible fluorescent probes for long-term noninvasive bioimaging application.[7,8] Nanomaterials with a combination of diagnostic and therapeutic functions into one theranostics systems are prominent these days and form an all-in-one approach.

Currently, lyotropic nano-liquid crystalline (NLC) phase particles are emerging as an attractive carrier system due to its ability to carry hydrophobic, hydrophilic as well as amphiphilic drugs.[9−11] Its peculiar high lipid volume fraction and ordered three-dimensional (3D) mesoporous internal structure, provides the greater stability and controlled release of the lipophilic

cargos compared to conventional liposomes, this attribute has made NLC's as a potential alternative delivery vehicle for pharmaceuticals.[12−14] Here we focus on inverse hexagonal (HII) phase liquid crystals for the development of multimodal nanoparticles ensemble of tumor-targeting, imaging and therapeutic properties simultaneously. We have designed a novel sigma receptor ligand, anisamide (AA)-grafted Pluronic F127 (PF127), using carbodiimide chemistry for the stabilization of glyceryl monooleate (GMO)-based nanoparticles (NLC NPs). Further, the AIE effect was imparted using tetraphenylethene (TPE), an iconic fluorogen in combination with a phytoestrogen, formononetin (FMN), for its spatiotemporal release.

TPE is a propeller-shaped molecule, which, in the dissolved state, possesses torsional motions capable of relaxing the energy of absorbed photons nonradiatively, whereas on aggregation, they promote efficient photoluminescence due to the restriction of their intramolecular rotations (RIR).[15,16] Although TPE has absorption maxima, emission spectra are located below the near-infrared (NIR) region. It was used to show that TPE has advantage over conventional organic dyes, which are highly emissive when dissolved, but once clustered in the nanoparticles, aggregation-caused quenching (ACQ) of fluorescence limits the doping amount of dyes, which cannot be swapped by simply increasing the amount of dye concentration. However, there are several reports, where, by modifying TPE with strong electron-donating groups or extending the conjugation length of the $\pi$-system, it shows increase in transient absorption in the NIR region (bathochromic shift).[17,18] Moreover, the major factor for the development of bioprobe for in vivo bioimaging is biocompatibility of the imaging agents. Other AIE system like anthracene derivatives are carcinogenic, and AIEgen metal complexes pose a daunting obstacle due to their intrinsic cytotoxicity.[19,20] Besides, the unique property to overcome the ACQ effect of conventional organic fluorophores, safety profile along with high "off−on" contrast ratio, large Stokes-shifted fluorescence, long luminescence lifetime, strong photobleaching resistance, and simple and cheap chemical synthesis of TPE-based materials have driven us to select TPE over other AIEgens.[21−23]

Embellishment of drug-delivery vehicle by AA like small molecular ligand enhances the tumor detection with high specificity.[24,25] They locate the overexpressed sigma receptors on breast cancer cells, and then the loaded smart optical beacon reports the cancer location by the way of fluorescent glow.[26] FMN (7-hydroxy-40-methoxyisoflavone) is a phytoestrogenic isoflavone proven to induce apoptosis, which inhibits cell proliferation and cell cycle progression in breast cancer, prostate cancer, and cervical cancer. Moreover, it possesses immunomodulatory, cardioprotective, and hypolipidemic activities.[27,28] Despite its prodigious biological outcomes, FMN bioactivity is highly limited due to low aqueous solubility (0.05 mg/mL) and extensive metabolism by glucuronidation and sulfation, which altogether attributed to its low systemic or target site concentrations and confined the clinical application.[29−31] It is thus envisaged to fabricate a stable, effective, and safe delivery system to circumvent the poor solubility and its collateral effects of FMN.

Throughout this article, it was shown that inverse hexagonal NLC NPs co-loaded with AIE fluorogen and an anticancer drug could be prepared and stabilized efficiently by the mixture of PF127/PF127-AA that give these nanoparticles superior targetability toward MDA-MB 231 and 4T1 cancer cells

concerning nontargeted nanoparticles. To the best of our knowledge, this is the first report of NLCs doped with FMN for antineoplastic activity. Furthermore, the extensive studies that were conducted will propound the aggregation-induced emission fluorogen-based NLC nanotheranostics for breast cancer therapy.

## 2. MATERIALS AND METHODS

**2.1. Materials.** *p*-Anisic acid, formononetin (FMN), glyceryl monooleate (GMO), Pluronic F127 (PF127), tetraphenylethylene (TPE), carbonyldiimidazole (CDI, 99%), (dimethylamino)pyridine (≥99%), dicyclohexylcarbodiimide (DCC, ≥99%), *N*-hydroxysuccinimide (NHS, 99%), 3-[4,5-dimethylthiazol-2-yl]-2,5-diphenyltetrazolium bromide (MTT), propidium iodide (PI), and RNase were purchased from Sigma-Aldrich (St. Louis, MO), whereas Annexin V apoptosis kit was obtained from Merck. High-performance liquid chromatography (HPLC) solvents, such as methanol, were purchased from Merck (India). All other chemical reagents were of analytical grade and obtained from commercial sources. Triple-distilled water was prepared from Milli-Q system (Millipore, Bedford).

**2.2. Methods.** *2.2.1. Synthesis and Characterization of Pluronic F127−Anisamide Conjugate (PF127-AA).* The conjugate between AA and PF127 was prepared by carbodiimide chemistry in the presence of DCC and NHS. In brief, amine-terminated PF127 (PF127-NH₂) and NHS-activated anisic acid (anisic acid-NHS) were separately prepared (see the Supporting information for the detailed synthesis procedure) and then anisic acid-NHS (44 mg, 0.176 mmol) was added gradually to PF127-NH₂ (500 mg, 0.0395 mmol) and triethylamine (3.95 mg, 0.0395 mmol) was dissolved in dichloromethane at 0 °C under constant stirring for 1 h. The reaction was allowed to proceed for 24 h at room temperature (RT). The resulting PF127-AA was recovered by precipitating in diethyl ether and dried in vacuum for 48 h. The product PF127-AA was characterized by proton NMR and Fourier transform infrared (FTIR) spectroscopy techniques (PerkinElmer Spectrum II). NMR spectra were recorded using Bruker DRX-300 (Bruker, Fallanden, Switzerland) at 300 MHz by dissolving in CDCl₃ and analyzed using TopSpin software package.

*2.2.2. NLC NPs Preparation.* GMO-based targeted liquid crystalline particles (AA-NLC-TF) were prepared by dispersing an appropriate amount of GMO in phosphate-buffered saline (PBS, pH 7.4) solution of PF127/PF127-AA mixture at 70 °C using an ultrasonic processor (Vibra-Cell VCX 750, Sonics & Materials. Inc.) attached with a microtip at 20% amplitude power for 10 min in pulse mode (5 s sonic pulses interrupted by 5 s breaks). Doped NLC NPs were obtained by dispersing the FMN (12.5 × 10⁻² wt %) and TPE (1.3 × 10⁻² wt %) in the melted GMO (60 mg/mL) before mixing with the Pluronic solution. The GMO and PF127/PF127-AA were mixed in a ratio of 92:8 by weight. The final concentration of PF127/PF127-AA in solution was around 0.46 wt %. Similarly, nontargeted nanoparticles (NLC-TF) were prepared using PF127 as a stabilizer. The resulting white milky dispersion was stored at RT for future experimentation.

*2.2.3. Determination of Loading (LE) and Entrapment Efficiency (EE) of NLC NPs.* The LE and EE of FMN and TPE in NLC-TF and AA-NLC-TF were determined by calculating the free and total amount of FMN and TPE in the formulation. Briefly, 2 mL of NLC dispersion was loaded into a dialysis membrane (molecular weight cut-off (MWCO) 12 kDa) and dialyzed against Milli-Q water (1000 mL) for 4 h at RT by replacing the water every 1 h. After 4 h, NLC dispersion purified from the nonencapsulated drug was obtained. A similar method was followed for the determination of TPE content. By disrupting the NLC NPs with acetonitrile/methanol mixture, FMN and TPE contents were quantified, respectively, at 259 and 361 nm using the validated RP-HPLC method (Shimadzu, Japan) (see the Supporting information for HPLC method).[32]

%LE was determined by eq 1

$$\%LE = \frac{W_{TP} - W_{UP}}{W_{TL}} \times 100$$

(1)

where $W_{TP}$, $W_{UP}$, and $W_{TL}$ are weights of total payload, unbound payload, and total lipid, respectively.

% EE was determined by eq 2

$$\%EE = \frac{W_{NLC}}{W_T} \times 100 \tag{2}$$

where $W_{NLC}$ is the weight of FMN/TPE entrapped in NLC and $W_T$ is the total weight of FMN/TPE added to the NLC formulation.

*2.2.4. Quasi-Elastic Light Scattering (QELS) Experiments.* At 25 ± 0.1 °C, the particle size and ζ potential of the nanoparticles were determined using Nano ZS 2000 (Malvern Instruments, Malvern, U.K.). The NLC formulations were diluted 1:100 times before the measurements of optimal sensitivity. All of the measurements were done in triplicate. The software available in Malvern Instruments (CONTIN algorithm) was used, and particle size values were reported as Z-average particle diameter. The width of hydrodynamic diameter distribution is indicated by polydispersity index (PDI).

*2.2.5. Small-Angle X-ray Scattering (SAXS) Studies for Phase Identification.* The phase identity and internal structure parameters of the NLC NPs were measured on a S3-Micro SAXS/SWAXS camera system (HECUS X-ray Systems, Graz, Austria) equipped with a one-dimensional position-sensitive detector (HECUS PSD50M) containing 1024 channels of width 54.0 μm. Cu Kα radiation (wavelength, 1.54 Å) was provided by a GeniX X-ray generator. Measurements were performed in quartz flow cell; the temperature was controlled by a Peltier system. Samples were maintained at 25 °C for 30 min before experimenting. The working q range used to detect signals was 0−0.6 Å$^{-1}$, where the length of scattering vector q is defined by eq 3.[33] The symmetry of the liquid crystalline nanoparticles was determined by the relative q positions of the Bragg peaks shown in the scattering curves. The water channel radius, $r_w$, of the inverse hexagonal (HII) phase of NLC NPs was calculated using eq 4.[13,34]

$$q = \left(\frac{4\pi}{\lambda}\right)\left(\frac{\sin\theta}{2}\right) \tag{3}$$

where θ is the scattering angle relative to the incident X-ray and λ is the wavelength at which X-rays are generated.

$$r_w = a(1 - \varnothing_{lip})^{1/2}\left(\frac{\sqrt{3}}{2\pi}\right)^{1/2} \tag{4}$$

where a is mean lattice parameter and $\varnothing_{lip}$ is the volume fraction of the dispersion phase.

*2.2.6. Morphological Evaluation of NLC NPs.* The morphology of NLC NPs was observed by various microscopic techniques.

*2.2.6.1. Transmission Electron Microscopy (TEM).* Briefly, the samples were placed over a carbon-coated copper grid and let to settle for 5 min. Then, the dried samples were negatively stained with 2% aqueous solution of uranyl acetate. Finally, the samples were observed on Jeol TEM 1400 (JEOL Ltd., Tokyo Japan).[35]

*2.2.6.2. Atomic Force Microscopy (AFM).* APE Research AFM (AFM, APCER, Italy) was used for the morphological evaluation of NLC NPs in a noncontact mode using cantilever (μmash NSC15/AIBS) of 125 μm length, 35 μm width, and <10 nm tip radius. Briefly, a drop of 10 μL of NLC samples was placed on a coverslip and allowed to air dry. After carefully removing the excess aqueous phase only and not allowing the sample to get completely dry, the samples were viewed under an atomic force microscope with a force constant of 45 N/m.[36−38]

*2.2.6.3. Cryogenic Force Emission Scanning Electron Microscopy (Cryo-FESEM).* For the morphological analysis using ZEISS ULTRA plus Cryo-FESEM (Carl Zeiss International, Germany), selected NLC formulations were transferred using a micropipette into brass rivets and plunge-frozen in liquid nitrogen at −190 °C (Alto 2500, Gatan) immediately. Subsequently, the samples were transferred under vacuum to the cryo-chamber of the microscope, where the temperature was maintained at −150 °C, followed by fracturing frozen samples using a knife maintained at −150 °C to reveal a clear surface. Then, the samples were sublimed for 15 min at −90 °C to

etch any water on its surface following fracture. Conductive platinum was used to sputter-coat at 11 mA for 50 s to deposit a thin layer on top of the sample. The sample was then transferred under vacuum into the Cryo-FESEM microscope chamber and imaged at an accelerating voltage of 3 kV and a working distance of 5−6 mm.

*2.2.7. Photophysical Characterization.* The photophysical characterization of NLC nanoparticulate dispersions was conducted by prior dilution with Milli-Q water (1:100). UV−vis absorption spectra were recorded using a UV-1700 PharmaSpec UV−vis spectrophotometer (Shimadzu Corporation, Tokyo, Japan). Fluorescence measurements were recorded on Agilent Cary Eclipse Fluorescence Spectrophotometer (Agilent Technologies, CA). The fluorescence quantum yields on TPE were measured using rhodamine 6G dissolved in ethanol as a standard ($\Phi_{ref}$ = 0.94).

*2.2.8. In Vitro Drug Release Studies.* The release of FMN and TPE from AA-NLC-TF was assessed using a dialysis bag method at 37 °C. In short, NLC NPs containing equivalent amount of FMN (2 mg) and TPE (0.2 mg) were loaded into a dialysis bag (Spectra/por, MWCO 12 kDa, CA) and then the bag was immersed in 100 mL of phosphate-buffered saline (PBS, pH 7.4 or pH 5.5) containing 0.1% v/v Tween 80 at 37 ± 0.5 °C to maintain sink condition and continuously rotated at 100 rpm. The samples were collected from the sink and replaced with fresh PBS at regular intervals. Finally, the concentrations of FMN and TPE were analyzed using the HPLC method. The release rate of the payload was calculated using eq 5

$$RR = \left(\frac{wd}{wD}\right) \times 100 \tag{5}$$

where wd is the amount of payload released after specific time point and wD is the total amount of payload used in the release study.[39]

*2.2.9. Stability Studies.* The physical stability of the optimized formulations was measured at 25 °C for change in the particle size and PDI at regular time intervals. Further, to determine the in vivo fate of AA-NLC-TF, the stability was measured in biologically relevant media by incubating the nanoparticles in 10% fetal bovine serum (FBS) and the changes in size with time were monitored using QELS.

*2.2.10. Hemolysis Assay.* Hemolytic toxicity study was performed according to a reported protocol with slight modifications.[40] Fresh blood was collected in heparinized vials centrifuged at 3000 rpm for 10 min to separate the red blood cells (RBCs). Sediment RBCs were washed with PBS (pH 7.4) and then diluted with PBS to obtain 2% hemocrit. Blank nanoparticles, free drug, NLC-TF, and AA-NLC-TF were incubated with equal volume of RBC suspension at a various concentrations of FMN for 2 h at 37 °C. After incubation, the samples were centrifuged for 10 min at 3000 rpm and the supernatants were drawn to quantify the hemoglobin content using a microplate reader (PowerWave XS, Biotek, VT) at 540 nm. RBC treated with 1% Triton-X served as positive, whereas PBS (pH 7.4) treated RBC served as negative control.

*2.2.11. Cell Culture.* MDA-MB 231, human breast cancer cell line, was obtained from American Type Culture Collection (Rockville, MD), whereas 4T1 cells were obtained from National Center for Cell Science (NCCS, Pune, India). Cells were cultured in Roswell Park Memorial Institute medium-1640 (RPMI-1640) with 10% (v/v) FBS, along with 100 μg/mL streptomycin and 100 U/mL penicillin. All of the cancerous cells were cultured in an incubator (Thermo Scientific) at 37 °C under 90% relative humidified environment of 5% $CO_2$.

*2.2.12. Cellular Cytotoxicity Studies.* In vitro cytotoxicity of free FMN, NLC formulation (blank NLC loaded with an imaging agent, NLC-TF, AA-NLC-TF) was assessed using 3-(4,5-dimethylthiazol-2-yl)-2,5-diphenyltetrazolium bromide (MTT) assay on MDA-MB 231 and 4T1 cells separately. In brief, MDA-MB 231 and 4T1 cells were seeded in 96-well plates separately (3 × 10$^3$ cells/well) in 100 μL of RPMI containing 10% FBS and kept for incubation at 37 °C in 5% $CO_2$. Experiments were carried out when cells had reached 90% confluence. The free drug and the different formulation of NLC were added to the cells in RPMI with 2% FBS at different concentrations (ranging from 1 to 60 μM equivalent concentration of FMN/TPE) and incubated for 48 h at 37 °C. After 48 h, media was removed and

cells were treated with 20 μL of MTT (5 mg/mL) reagent for 4 h. Then, 100 μL of dimethyl sulfoxide (DMSO) was added to dissolve the formed formazan crystals. The color developed was measured on an automated microplate reader at 570 nm, and its absorbance is proportional to the number of viable cells. Untreated cells served as a control in comparison to the treated cells, and the results are shown as the percentage of cell viability. All experiments were carried out thrice ($n = 3$). Data were expressed as a mean ± standard deviation (SD).

Cytotoxicities of blank and AA-NLC-TF NLC NPs were also determined on J774.2 cells to evaluate the biosafety of the developed liquid crystalline particles.

*2.2.13. Cellular Uptake and Cell Imaging Studies. 2.2.13.1. Confocal Laser Scanning Microscopy (CLSM).* The application of anisamide-conjugated NLC NPs was investigated for the targeted intracellular imaging as well as cellular uptake by confocal microscopy. MDA-MB 231 cells and 4T1 cells were seeded on polylysine-coated coverslips placed in 12-well plates at a density of $2 \times 10^4$ cells per well in 1 mL of RPMI with 10% FBS and incubated for 24 h. The cells were then treated with media containing AA-NLC-TF and NLC-TF particles at equivalent concentrations of TPE (0.25 μM), FMN (3 μM), and rhodamine B (20 μM) incubated for 4 and 12 h. After incubation, excess nanoparticles were removed by washing with PBS and then cells were fixed with 4% formaldehyde solution for 15 min at RT. Finally, the coverslips were mounted on the glass slides sealed with mounting media and observed under a confocal microscope (Carl Zeiss LSM510 META, Carl Zeiss, Germany). Plan-Apochromat 63×/1.40 oil DIC objective lens with an excitation of 405 nm for TPE (argon 405/488 laser lines) and 561 nm for rhodamine B (diode-pumped solid-state laser lines), bandpass filter 420−480, and long pass filter 575 were used.

*2.2.13.2. Flow Cytometry.* For the assessment of quantitative uptake of nanoparticles by MBA-MB 231 and 4T1 cells, flow cytometer (BD Biosciences, FACSAria, Germany) was utilized. The cells were seeded at a density of $5 \times 10^5$ cells per well in a six-well plate and incubated for 24 h, followed by treatment with the formulation described above. Following incubation for the respective time intervals, the cells were washed with PBS, harvested, and then suspended in 0.5 mL of PBS. Cell-associated fluorescence was used for the quantitative determination of nanoparticles uptake using 405 nm laser with a 450/20 bandpass filter to collect the data. The receptor specificity of the AA-NLC-TF nanoparticles was further evaluated through receptor blocking studies using flow cytometry. MDA-MB 231 cells were preincubated in 100 μM AA in complete media for 2 h before the addition of the above-mentioned NLC NPs.

*2.2.14. Cell Cycle Analysis.* For the cell arrest, propidium iodide (PI)-based assay was used to evaluate the effect of FMN on MDA-MB 231 cells by employing a flow cytometer (BD Biosciences, FACSCalibur, Germany). MDA-MB 231 cells were grown in six-well plates ($1 \times 10^6$ cells/well) and incubated overnight at 37 °C. Adherent cells were treated with free FMN, NLC formulations containing an equivalent concentration of FMN (3 μM) along with fresh media and incubated for 24 h. After a predefined time interval, the cells were washed, harvested, and fixed with the precooled ethanol (70%) at 4 °C for 2 h. After fixing, the cells were centrifuged and resuspended in 500 μL of PBS (pH 7.4) and treated with ribonuclease A (100 μg/mL) and PI (50 μg/mL) for 30 min in the dark. Cell-based fluorescence was measured using a flow cytometer to appraise the phases of cell cycle arrest.

*2.2.15. Apoptosis.* MDA-MB 231 cells were incubated at a density of $1 \times 10^5$ per well in a six-well plate for 24 h and treated with media containing different treatments of FMN equivalent to (3 μM). After 48 h incubation, the cells were harvested, washed with PBS twice, collected, and resuspended in 500 μL of 1× binding buffer and stained with Annexin V−fluorescein isothiocyanate (FITC) (5 μL) and propidium iodide (10 μL) for 20 min under dark conditions and analyzed for early and late apoptosis using a flow cytometer (BD Biosciences, FACSCalibur, Germany). Untreated cells were used as control over treated cells. The experiments were done in triplicate.

*2.2.16. Mitochondrial Membrane Potential (MMP).* To measure MMP of MDA-MB 231 cells, JC-1 dye (5,5′,6,6′-tetrachloro-1,1′,3,3′-

tetraethylbenzimidazolylcarbocyanine iodide) (Molecular Probes, Eugene, OR) was used. Initially, the cells were grown in 12-well plates at a density of $1 \times 10^5$ cells/well, followed by treatment with free FMN, blank NLC, and targeted and nontargeted nanoparticles at an equivalent drug concentration of FMN (3 μM) for predetermined time intervals. Subsequently, media was removed and cells were washed with PBS and treated with JC-1 solution (15 μg/mL). Cell-associated fluorescence was measured by the flow cytometer. PBS-treated cells served as negative control, whereas 50 nM carbonyl cyanide 4-(trifluoromethoxy) phenylhydrazone (FCCP)-treated cells were used as positive control.

*2.2.17. Reactive Oxygen Species (ROS) Generation.* Dichloro-dihydro-fluorescein diacetate (DCFH-DA) assay was performed to determine the ROS levels in the treated cells. Briefly, MDA-MB 231 cells ($2 \times 10^5$ cells/well) were grown in six-well plates and then treated with 3 μM equivalent FMN containing NLC formulation, free drug, and blank NLC. After 12 and 24 h of treatment, the cells were exposed to 10 μM DCFH-DA and incubated for 0.5 h at 37 °C. After incubation, the cells were washed twice with PBS, trypsinized, and resuspended in PBS. Finally, the ROS production level was determined by the fluorescence intensity of dichlorofluorescein (DCF) using the flow cytometer (BD Biosciences, FACSCalibur, Germany). Untreated cells were used as control, and all of the experiments were repeated thrice ($n = 3$).

*2.2.18. In Vivo Studies.* All of the animals were obtained from the National Laboratory Animal Center (NLAC) facility, CSIR-Central Drug Research Institute (CDRI), Lucknow. All of the animal experiments were done with prior approval (IAEC approval No. IAEC/2017/159) by the Institutional Animal Ethical Committee (IAEC) of CSIR-CDRI, India.

*2.2.19. Tumor Model.* Female BALB/c mice (4 weeks old; weight, 18−20 g) were selected and acclimatized for a week in 12 h light and dark condition under controlled temperature (24 °C). The mice were injected subcutaneously with about 100 μL of cell suspension containing $5 \times 10^6$ 4T1 cells at the mammary gland near to the lower right quadrant of the abdomen. After inoculation, regular observation of animals was made, and when the tumor grew to about 100 mm³, studies were started.[41]

*2.2.20. In Vivo Optical Imaging.* An in vivo imaging system was used to study the accumulation of AA-NLC-TF in the tumor-bearing mice inoculated with 4T1 cells. NLC-TF and AA-NLC-TF containing (10 mg FMN equiv/kg) and PBS were intravenously (iv) administered when tumors reached about 100 mm³ in volume. The mice were anesthetized with 2% isoflurane/air mixture, and in vivo optical images were taken within the predetermined time with an excitation filter of 430 nm and an emission filter of 620 nm. The exposure time was 5 s per image. The final concentration of TPE used was 1 mg/kg. Signal intensity of the images was quantified as the radiant efficiency within a region of interest prescribed over the tumor site. After imaging, the mice were sacrificed and the major organs of tumor, brain, heart, lungs, liver, spleen, and kidney were harvested and imaged under the same conditions to know the distribution of nanoparticles. Fluorescence images of the mice were acquired with the IVIS Kinetic Imaging System (Caliper Life Sciences), and the images were analyzed with Living Image software version 4.4 (Caliper Life Sciences).

*2.2.21. In Vivo Antitumor Efficacy.* For in vivo antitumor efficacy studies, the mice were divided into four groups with six animals in each group under regular observation once. When tumor volume reached 100 mm³, the mice were injected with iv route free FMN, NLC-TF, AA-NLC-TF (at an equivalent dose of 10 mg/kg FMN), and PBS as control every 2 days for seven times. Tumor volumes were measured for individual animals in all experiments every 2 days with a digital caliper in two dimensions and calculated using the following formula: volume = (length × width²)/2. The mice were sacrificed on the 20th day, and the tumors were weighed to calculate the tumor growth inhibition rate (TIR) by the following formula: TIR = {(1 − (mean volume of treated tumors)/mean volume of control tumors)} × 100%.

*2.2.22. Survival Analysis.* For the survival analysis, the animals were divided into four groups similar to the tumor regression study, and six

**Scheme 1. Schematic Illustration of Synthetic Steps for PF127-AA and Schematic Illustration of AIE-Based Active Bioimaging in Vitro and in Vivo**
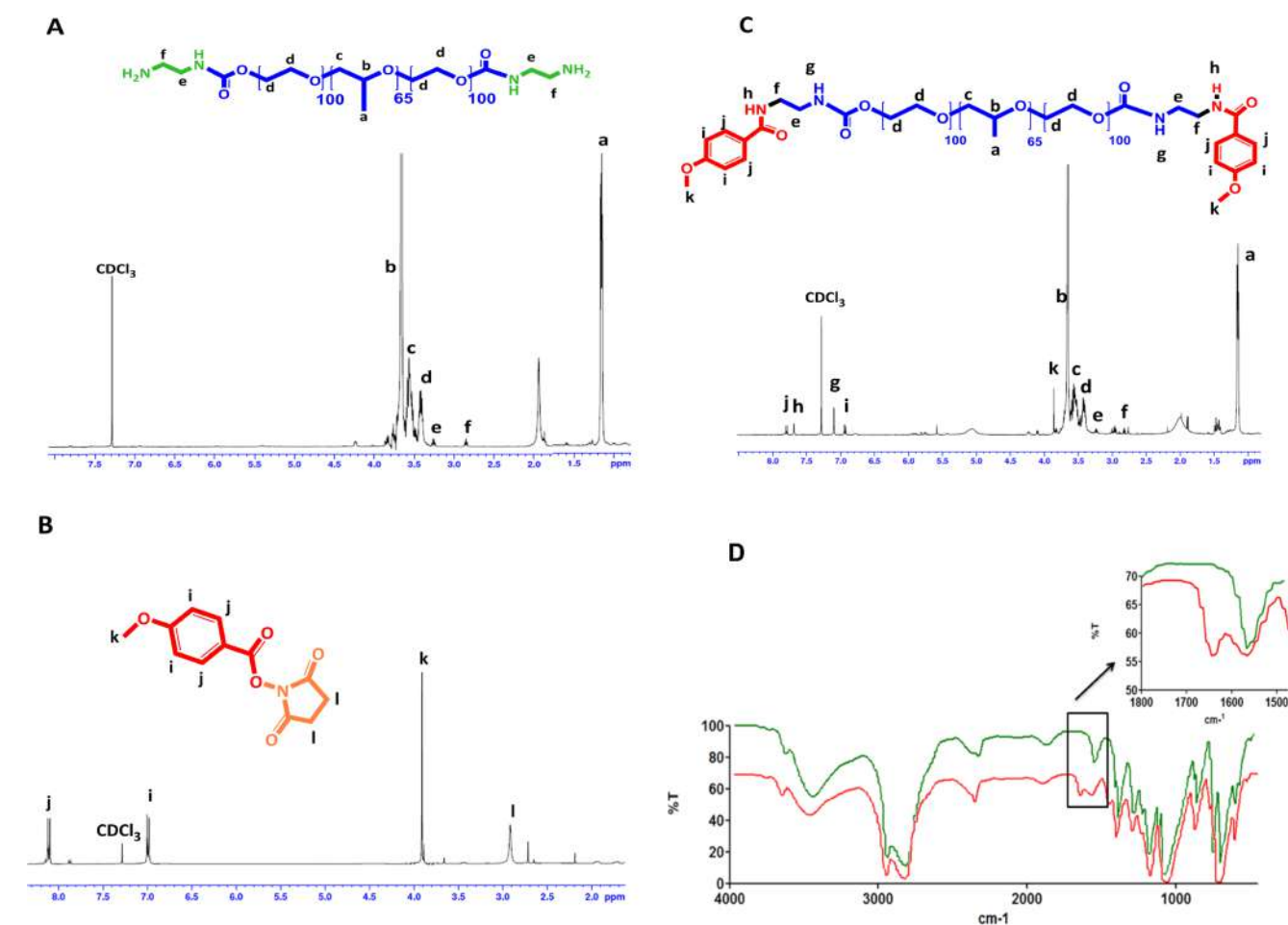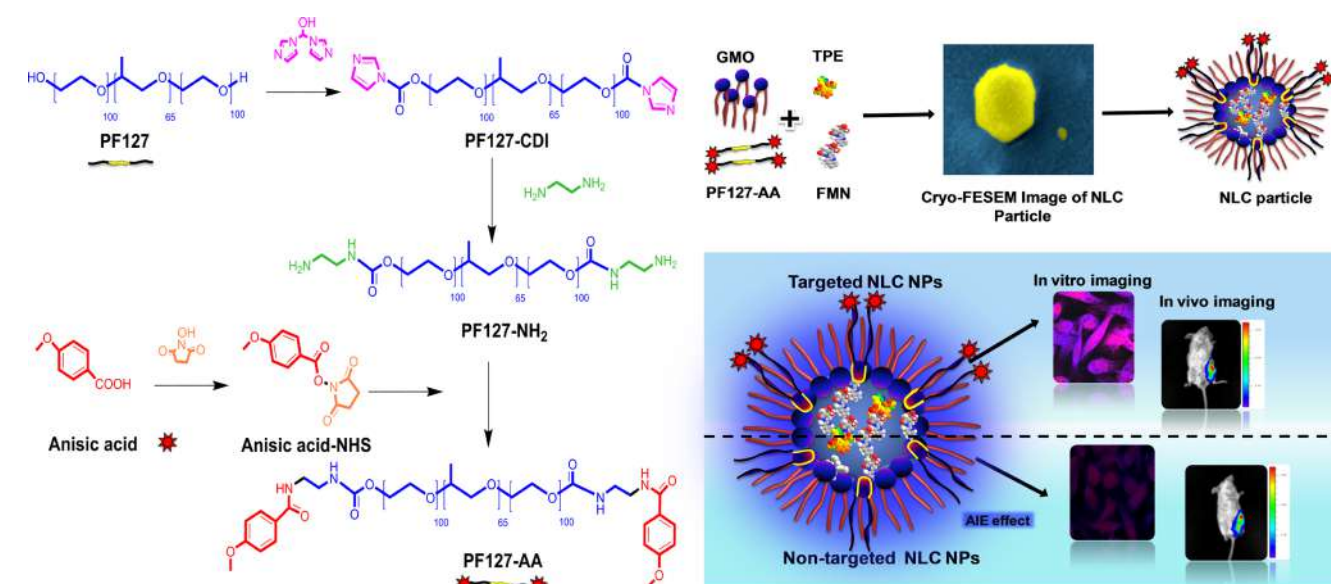




**Figure 1.** Characterization of conjugate by $^1$H NMR (A) PF127-NH$_2$; (B) anisic acid-NHS; (C) PF127-AA; and (D) FTIR spectra of PF127-AA.

animals were taken in each group for a separate experiment. The animals were observed daily when the tumor volume reaches 100 mm$^3$; treatment started as per the protocol mentioned above, and survival analysis study was conducted for up to 30 days. The survival rate of animals in these four different groups was measured during this

period and analyzed using GraphPad Prism 5.0 software. Survival curves were evaluated using the log-rank (Mantel−Cox) test method.

*2.2.23. Statistics.* Statistical significance of the data was analyzed by one-way analysis of variance, and probability values <0.001 or <0.05 were considered significant. All of the calculations were done using the

**Table 1. Characteristics of NLC NPs**[a]

| NLC NPs | particle size (nm) | PDI | $\zeta$ potential (mV) | % LE | | % EE | |
| --- | --- | --- | --- | --- | --- | --- | --- |
| | | | | TPE | FMN | TPE | FMN |
| blank | $112.0 \pm 5.36$ | $0.258 \pm 0.03$ | $-25 \pm 2.09$ | | | | |
| NLC-TF | $115.7 \pm 4.36$ | $0.101 \pm 0.012$ | $-22 \pm 1.28$ | $0.22 \pm 0.03$ | $2.12 \pm 0.06$ | $96 \pm 2.15$ | $96 \pm 3.20$ |
| AA-NLC-TF | $127.0 \pm 6.95$ | $0.242 \pm 0.015$ | $-24 \pm 2.56$ | $0.21 \pm 0.01$ | $2.15 \pm 0.03$ | $95.27 \pm 1.15$ | $97 \pm 2.89$ |

[a]All values are represented as mean $\pm$ SD.
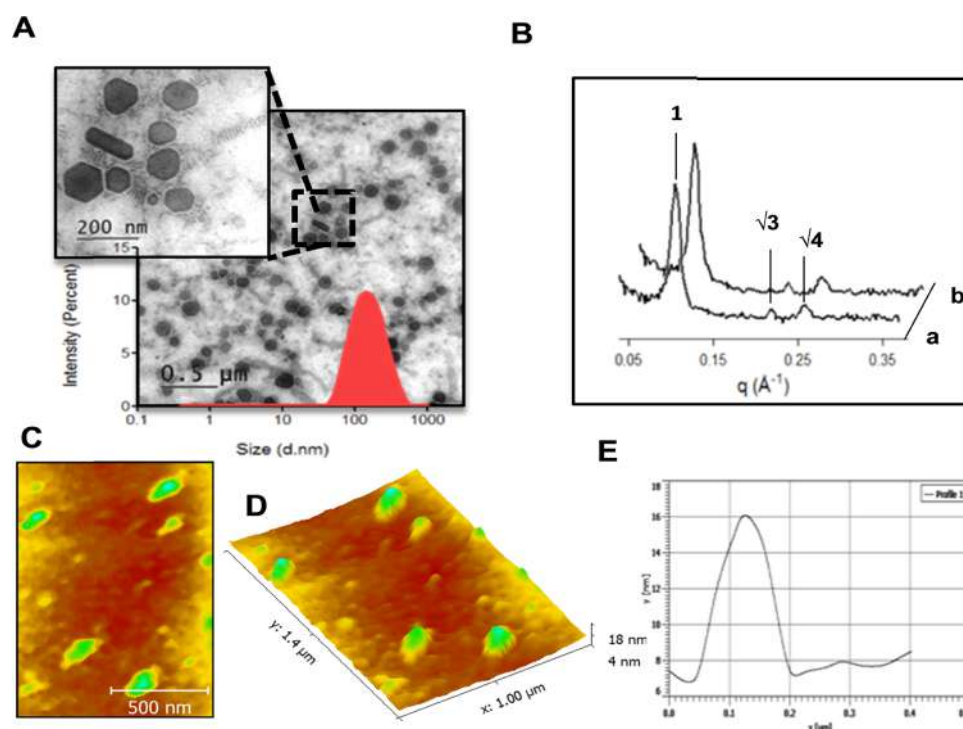


**Figure 2.** Size and morphological characterization of NLC NPs by (A) TEM (scale bar, 200 nm) and particle size distribution of AA-NLC-TF particles. (B) SAXS intensity plots of (a) blank NLC particles and (b) AA-NLC-TF. AFM images of AA-NLC-TF particles (C) two-dimensional image (scale bar, 500 nm) and (D) 3D view. (E) Height profile.

GraphPad Prism version 5.0 for Windows (GraphPad Software, San Diego, CA).

## 3. RESULTS

**3.1. Preparation of AIE Fluorogen-Based Targeted and Nontargeted NLC Nanotheranostics.** Here, we attempted to formulate the nanotheranostics to track down the tumor location and for chemotherapy. For this purpose, GMO-based NLC NPs stabilized by PF127/PF127-AA mixture was loaded with the FMN and TPE. The synthetic scheme and proposed model illustrating the AIE-based active bioimaging in vitro and in vivo are shown in Scheme 1. In brief, PF127-NH$_2$ was synthesized in the presence of CDI and ethylenediamine, and the conjugation of the amino group to the PF127 terminal was confirmed by the trinitrobenzene sulfonic acid assay (conjugation efficiency, 97%). Then, anisic acid-NHS was reacted with the amino end of PF127 to form PF127-AA. The successful conjugation of anisic acid to PF127-NH$_2$ was confirmed by $^1$H NMR spectra, where the singlet peak at 7.10 ppm was the characteristic peak due to the amidic NH from the precursor PF127-NH$_2$ conjugate, whereas the peak at 7.68 ppm was due to the just formed amidic bond with anisic acid-NHS. Also, FTIR spectrum of PF127-AA, which displayed the carbonyl group of the amidic function at 1715.3 cm$^{-1}$, attested the presence of anisamide in the polymer chain. By dissolving a known amount of PF127-AA in DMSO, UV absorbance at 260 nm was measured to determine the concentration of conjugated anisamide based on the calibration curve of anisamide plotted at 260 nm. The conjugation percentage of anisamide to PF127 was 94%. Subsequently, PF127 or PF127/PF127-AA mixture was used for the stabilization of GMO-based targeted and nontargeted NLC NP dispersions. $^1$H NMR spectra of the reactants and synthesized PF127-AA are presented in Figure 1.

**3.2. Physicochemical Characterization of NLC NPs.** First, the QELS method was used to determine the size and $\zeta$ potential of the nanoparticles. Results reported in Table 1 showed that a slight change in the hydrodynamic radii of nanoparticles was observed in QELS study. The mean particle size increased from 115.7 nm (100% PF127) to 127 nm (67% PF127 and 33% PF127-AA mixture) owing to increase in the amount of PF127-AA, and this growth suggested that the conjugation of anisamide to the PF127 modified the original steric stabilizing properties of the surfactant. Nonetheless, such a conjugation does not destabilize the nanoparticle delivery system. Thus, there were no major changes in the size and PDI of the NLC NPs during stability studies. The size of the nanoparticles obtained was also suitable for accumulation at the tumor site by enhanced permeability and retention effect, and they were found to be in good agreement with the dimensions
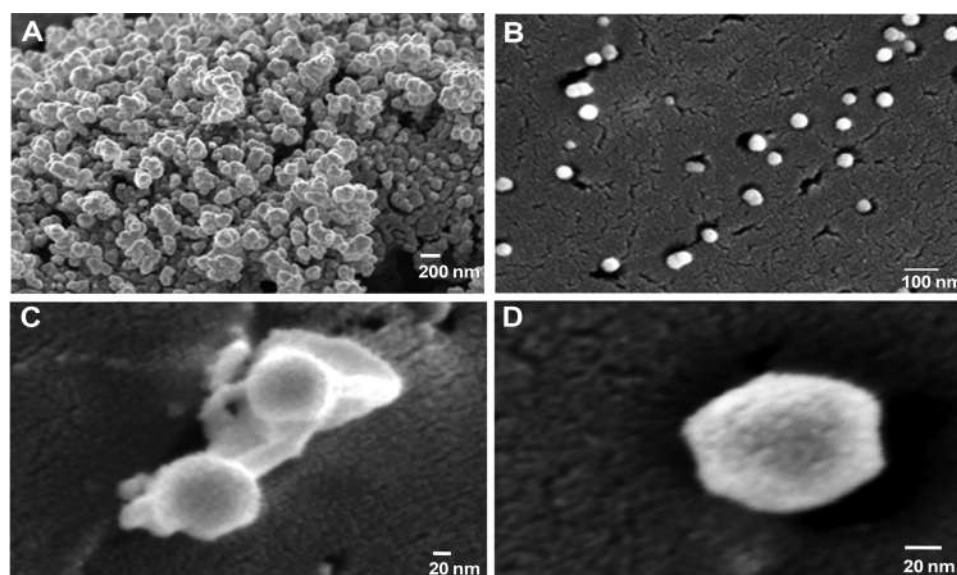
**Figure 3.** Cryo-FESEM photoimages of NLC NPs: blank nanoparticles (A) before dilution (scale bar, 200 nm) and (B) after dilution (scale bar, 100 nm); (C) blank nanoparticles (scale bar, 20 nm); and (D) AA-NLC-TF nanoparticles (scale bar, 20 nm).

obtained with Cryo-FESEM, TEM, and AFM images (Figures 2 and 3). After loading the drug and AIEgen, ascribed to their hydrophobic nature, they strongly intercalated within the lipid core of the NLC NPs The entrapment efficiencies (EE) of the drug and AIEgen in AA-NLC-TF were found to be 95 and 97% (Table 1), respectively. Pertaining to measured $\zeta$ potential values, they were found to be in the range of −22 to −25 mV. Although GMO, PF127, and PF127-AA do not carry any inherent charge, on the other hand, the negative charge of the nanoparticles could be due to the adsorption of the hydroxide ions of the polarized water layer surrounding its outer surface.[42]

Further, we have investigated the phase at which liquid crystalline particles exist through SAXS analysis. As can be seen from the SAXS data (Figure 2B), the Bragg peaks positioned at $1:\sqrt{3}:\sqrt{4}$ ratio represent an HII phase, the targeted nanoparticles (AA-NLC-TF) retained the hexagonal structure found in the blank NLC prepared with the 100% PF127 with no significant change in the lattice parameter even after substituted with 67% PF127 and 33% PF127-AA mixture as well as due to loaded cargo (FMN and TPE). Structural parameters like lattice parameters and water channel radii of NLC NPs are reported in Table 2.

**Table 2. Structural Parameters of NLC NPs Determined at 25 °C[a]**

| NLC NPs | lattice parameter, $a$ (Å) | water channel radii, $r_w$ (Å) |
|---|---|---|
| blank particles | 59.4 ± 0.4 | 31.0 ± 0.3 |
| AA-NLC-TF | 61.0 ± 0.2 | 33.1 ± 0.2 |

[a]All values are represented as mean ± SD.

**3.3. Morphological Evaluation of NLC NPs.** In this study, we have employed TEM, AFM, and Cryo-FESEM to observe the morphology of NLC NPs. Inspection of NLC particles through TEM revealed that the particles possessed hexagonal symmetry. Typically, HII phase liquid crystalline particles consist of water-filled continuous cylindrical lipid matrix arranged in the hexagon shape, and as shown in the TEM photoimage (Figure 2A), when viewed in two dimensions, the lateral view of these NLC NPs will be

observed as a rod-shaped particle. These nanoparticles have also been imaged by AFM, where the size and morphology of the particles showed broad agreement with the TEM images (Figure 2C−E). Concerning development in the field of electron microscopy, Cryo-FESEM is used to determine the interparticle structure as well as three-dimensional (3D) image of the dispersed liquid crystalline particles.[43,44] Usually, information on interparticle confined nanostructure is obtained when using Cryo-TEM, which is a widely used method for characterization of a variety of self-assembled nanostructures as a complement to QELS, SAXS, or SANS. Conduciveness of Cryo-FESEM technique allows vitrified samples to be imaged as same as Cryo-TEM, but sublimation of surface water and sputter-coated platinum reveals the 3D structure of nanoparticles. The 3D view exposed by the Cryo-FESEM showed that the NLC NPs adopted a hexagon-like structure as observed in TEM images (Figure 3). The average sizes obtained from the different techniques are 98.30−135.5 nm (TEM), 110.0−133.2 nm (AFM), and 90−140 nm (Cryo-FESEM).

**3.4. Photophysical Studies.** After the fabrication of nanoparticles, it is necessary to confirm the yielded nanoparticles capable of preserving the AIE effect. As shown in Figure 4A, due to the AIE property of TPE trapped in the crystalline core, liquid crystalline particles show bright blue emission under 365 nm UV light. Indeed, high-fluorescence quantum yield (0.29) was obtained for the TPE loaded in the nanoparticles. The presence of AA-NLC-TF nanoparticles in water was also confirmed by shining a laser beam through the nanoparticle solution to observe the Tyndall effect (Figure 4C). The absorption and fluorescence emission spectra of AA-NLC-TF were measured and are shown in Figure 4D,E. The peak shown at 342 nm might be attributed to the characteristic peak of TPE aggregates in water, and at the same equivalent concentration in NLC, the blue shift of the TPE peak is due to restriction of the intramolecular rotation (RIR) of the phenyl groups as well as the increased hydrophobicity of the local environment due to nanoaggregates. The maximum absorption and emission peaks of the liquid crystalline particles are found at 372 and 476 nm, respectively. This large Stokes shift (>104 nm), which can minimize the interference from the self-
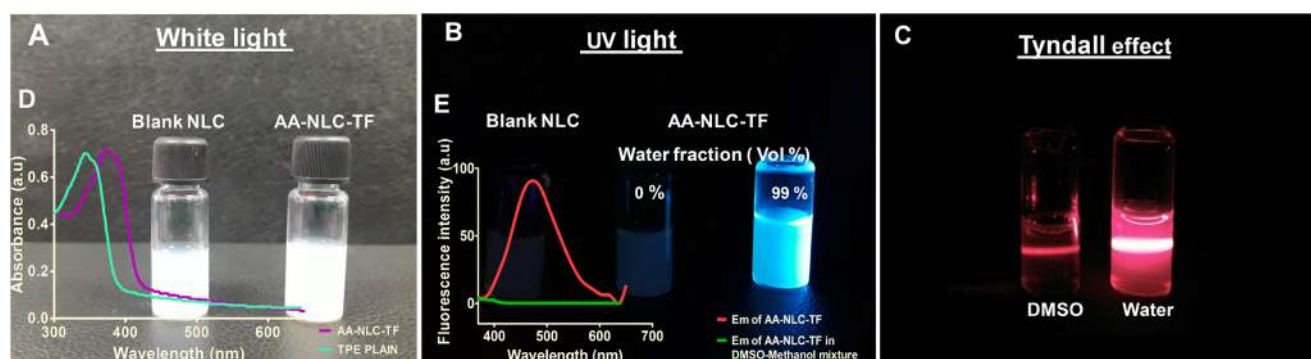
**Figure 4.** Fluorescence photographs of NLC dispersion (A) without UV illumination and (B) upon UV illumination (365 nm) and dispersion in DMSO and DMSO/water mixture (99 vol % of water), showing a typical AIE phenomenon. (C) Tyndall effect of AA-NLC-TF in DMSO and water. (D) Absorption spectrum of TPE plain and AA-NLC-TF. (E) Fluorescence spectrum of AA-NLC-TF in water and DMSO/methanol mixture excited at wavelength of 330 nm.
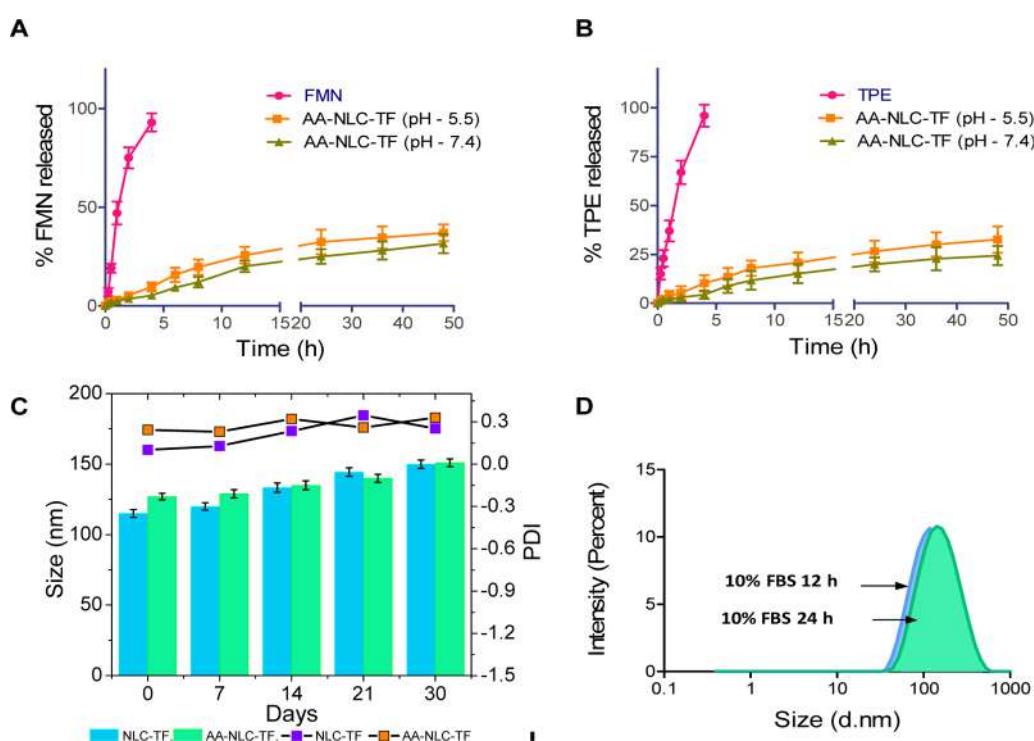


**Figure 5.** In vitro drug release profiles of (A) FMN from AA-NLC-TF and (B) TPE from AA-NLC-TF. Drug release study was conducted in PBS (pHs 7.4 and 5.5 at 37 °C) supplemented with 1% v/v Tween 80. (C) Data representing the physical stability of NLC-TF and AA-NLC-TF carried out in PBS (pH 7.4) at 25 °C for a period of 1 month. (D) serum stability of AA-NLC-TF for 12 and 24 h. Data are represented as mean ± SD of three experiments.

absorption, indicates the suitability of AA-NLC-TF nanoparticles for the potential bioimaging application.

**3.5. In Vitro Drug Release Studies.** The release profiles of FMN and TPE from AA-NLC-TF were recorded at two different pHs (7.4 and 5.5) using dialysis bag method to simulate blood and tumor-associated microenvironment. Free FMN and TPE dissolved in DMSO were also utilized as control, and a complete release (90.23 ± 3.60% for FMN and 95.78 ± 2.70% for TPE) within 4 h was found for both the payloads. But FMN and TPE encapsulated in AA-NLC-TF showed a controlled release without burst release at both the pHs, and it was observed that the release of payloads at pH 5.5 was faintly faster than that at pH 7.4. Approximately, 37.82 ± 3.22% of FMN was released at pH 5.5 in 48 h, whereas at pH 7.4, 30.90 ± 3.60% was found to be released. However, in case

of TPE, 32.60 ± 2.80 and 24.39 ± 2.30% were found to be released at pHs 5.5 and 7.4, respectively, within 48 h. Increase in release at pH 5.5 can be attributed to phase inversion of the liquid crystalline nanoparticles under acidic condition (Figure 5A,B). However, this phenomenon will be beneficial under actual disease conditions for the NLC NPs to show better anticancer effect.

**3.6. Stability Studies.** The physical stability of the nanoparticles due to steric stabilizer PF127 does not change, whereas the content of PF127-AA increased in the AA-NLC-TF formulation. This was evident by the monitored size and PDI of the nanoparticles on stability studies conducted at 25 °C for 1 month in PBS (pH 7.4). As shown in Figure 5C, there was no aggregation or change in the size and PDI of the NLC NPs, which indicates the long-term storage stability of the
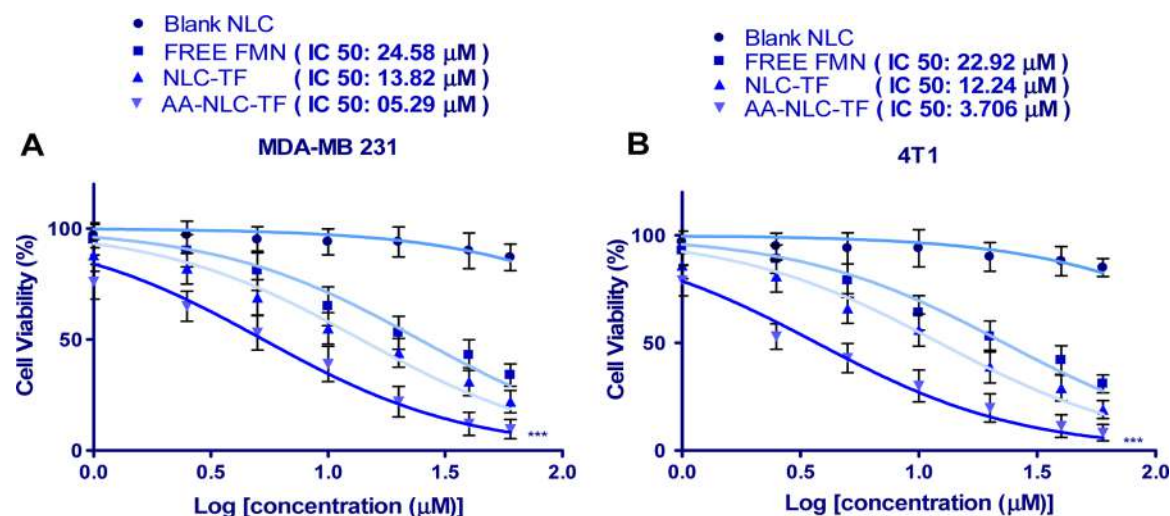
**Figure 6.** In vitro cell cytotoxicity analysis of (A) MDA-MB 231 and (B) 4T1 cells after treated 48 h with blank NLC NPs consisting of TPE equivalent to 1−60 $\mu$M, free FMN, NLC-TF, and AA-NLC-TF having FMN concentration equivalent to 1−60 $\mu$M. ***$P < 0.001$ vs the same dose of NLC-TF.
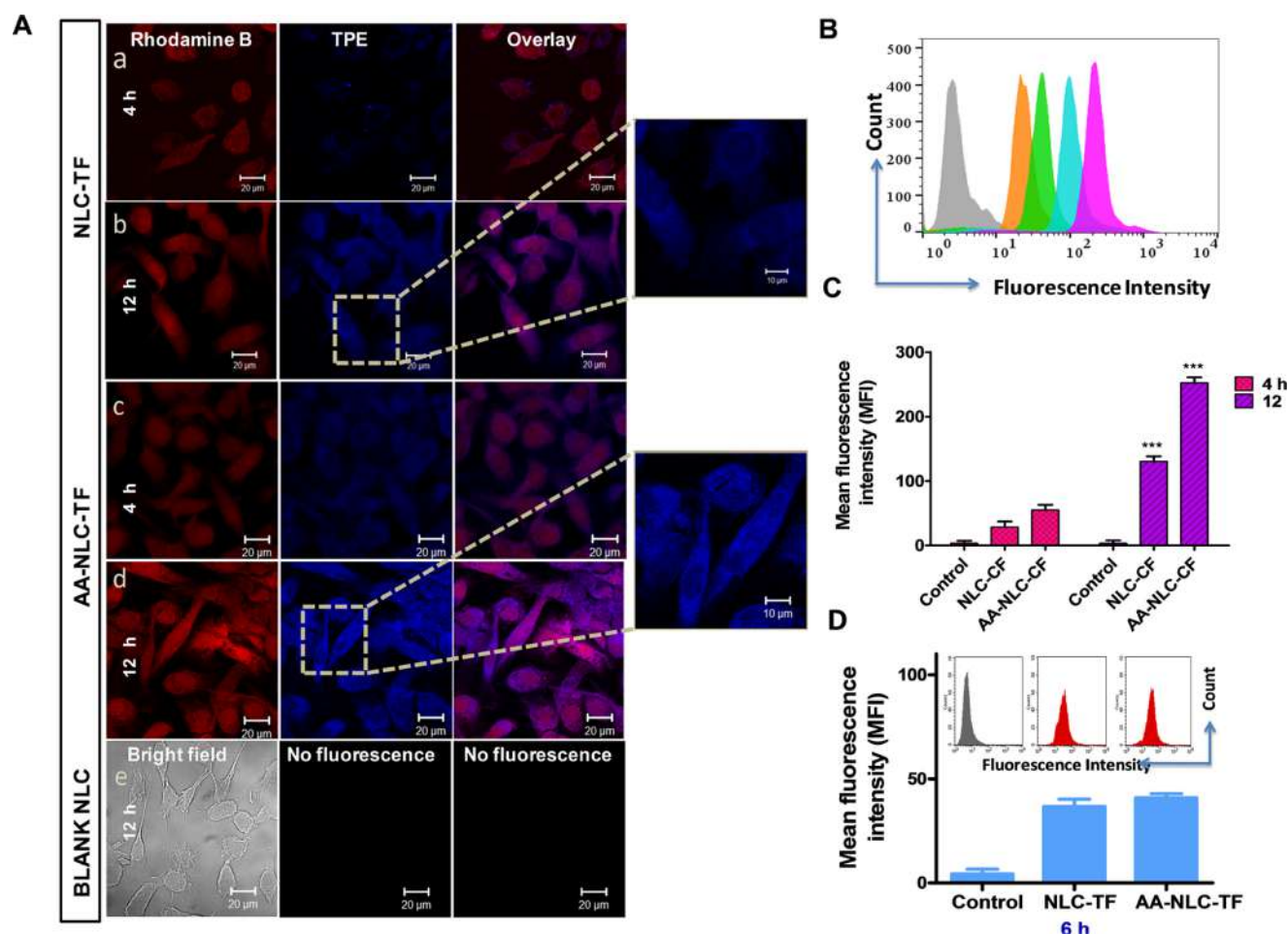


**Figure 7.** (A) CLSM images of live MDA-MB 231 cells treated with (a, b) AA-NLC-TF and (c, d) NLC-TF for 4 and 12 h; (e) blank NLC (scale bar, 20 $\mu$m). (B) Fluorescence intensity histograms of MDA-MB 231 incubated with AA-NLC-TF and NLC-TF (gray: control; 4 h group (orange: NLC-TF, green: AA-NLC-TF); and 12 h group (blue: NLC-TF, pink: AA-NLC-TF). (C) Mean fluorescence intensity values of MDA-MB 231 cells after 4 and 12 h incubation of AA-NLC-TF and NLC-TF with equivalent concentrations of TPE (0.25 $\mu$M) and FMN (3 $\mu$M). (D) Receptor blocking studies carried out using flow cytometer showing the fluorescence intensity histogram and mean fluorescence intensity values of MDA-MB 231 cells after 6 h incubation of AA-NLC-TF and NLC-TF nanoparticles.
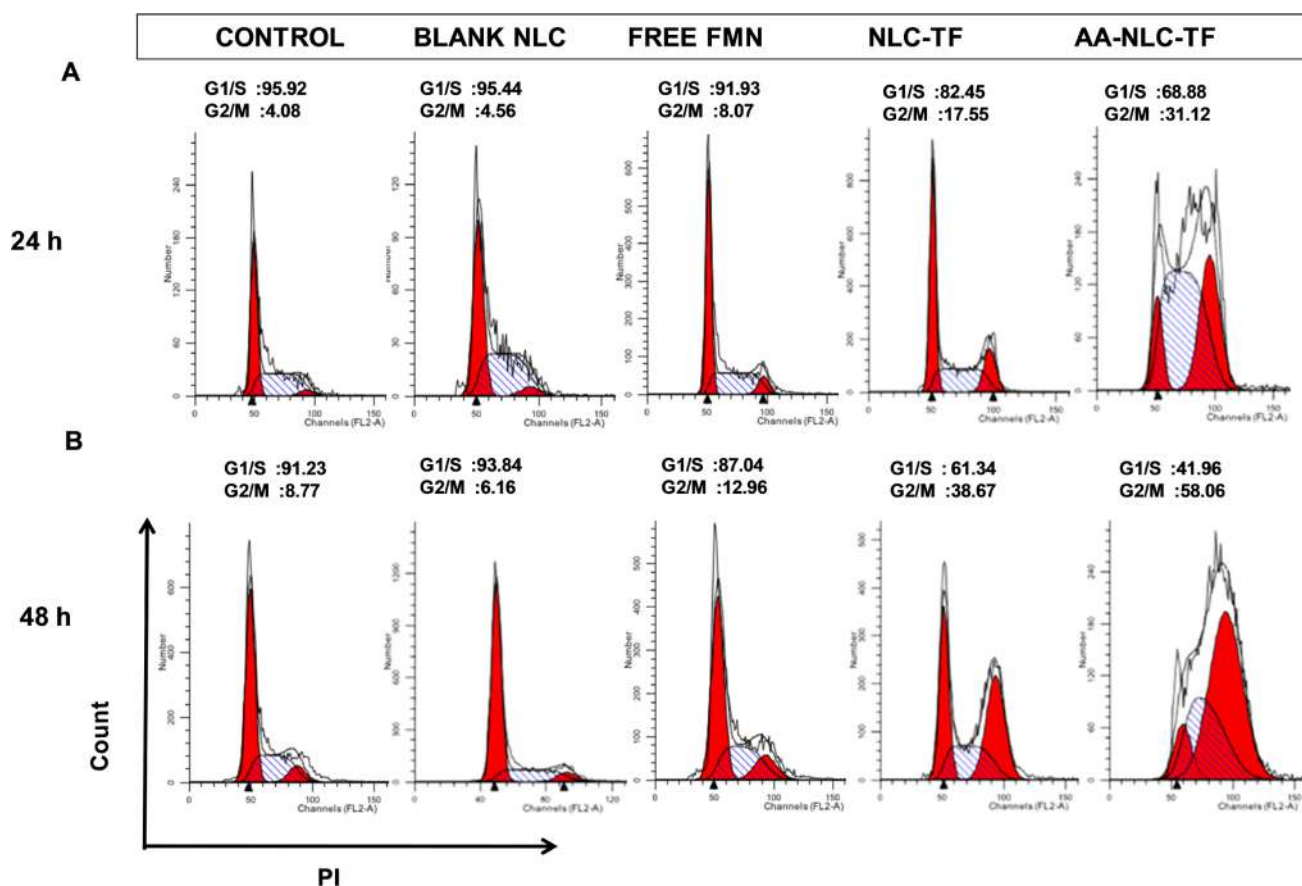
**Figure 8.** Representative cell cycle distribution in MDA-MB 231 cells (A) 24 h and (B) 48 h after incubation with blank NLC, free FMN, NLC-TF, and AA-NLC-TF at equivalent concentration of FMN (3 $\mu$M).

formulation. Moreover, the biological stability of AA-NLC-TF was also analyzed in serum. The size of AA-NLC-TF nanoparticles was monitored in the presence of 10% FBS. If nanoparticles aggregate in serum, then they might aggregate upon injection also. As shown in Figure 5D, size of the particles remained stable upon 12 and 24 h incubation in serum, which indicates that the physical stability of NLC NPs does not alter upon interaction with serum proteins.

**3.7. In Vitro Hemolytic Potential.** Hemocompatibility assay of formulations was performed to know the in vitro toxicity, which also serves as a simple measure for predicting the blood compatibility for in vivo experimentation. Formulations containing equivalent concentration range of 5−30 $\mu$M of FMN was used to assess the hemolytic potential of NLC formulation. FMN-loaded AA-NLC-TF showed (4.1 ± 1.3%) hemolysis at the highest equivalent concentration of FMN (30 $\mu$M), and all of the drug-loaded nanoparticles showed lower hemolysis at different equivalent concentrations of FMN in comparison to positive control. These results manifested the hemocompatibility of AA-NLC-TF toward in vivo experimentation (Figure S1).

**3.8. Cellular Cytotoxicity.** To assess the anticancer activity of the free FMN and FMN containing formulation, MDA-MB 231 and 4T1 cell lines were chosen. As shown in Figure 6. FMN, NLC-TF, and AA-NLC-TF showed dose-dependent loss of cell viability in MDA-MB-231 and 4T1 cell lines. The cytotoxicity of cells treated with NLC-CF was greater than that of free FMN in both the cell lines but lesser than that of AA-NLC-TF treatment. The half-maximal inhibitory concentration

($IC_{50}$) values of AA-NLC-TF nanoparticles were 4.64 and 2.61 folds less than those of the free FMN and NLC-TF after 48 h treatment in MDA-MB 231. Similarly, AA-NLC-TF showed 6.18 and 3.30 folds lesser $IC_{50}$ than free FMN and NLC-TF in 4T1 cells, respectively. These results suggest that the anisamide conjugation with NLC particles amplified the therapeutic effect of the FMN by targeted drugs in the MDA-MB 231 and 4T1 cells. Additionally, biosafety of blank NLC and AA-NLC-TF was evaluated on J774.2 cells, and the results proved that this formulation is safe for normal cells and also demonstrated the targeted toxicity toward cancer cells (Figure S2). MTT assay was used to assess the cytotoxicity, and nonlinear regression analysis was used to calculate the $IC_{50}$ values of the NLC NPs.

**3.9. Cell Imaging and Intracellular Spatial Distribution of NLC NPs.** Particulate uptake of nanocarrier by cancerous cells was confirmed by CLSM and flow cytometry. High sigma receptor expressing human breast cancer cell lines like MDA-MB 231 were selected for the uptake studies. The cells were treated with AA-NLC-TF and NLC-TF and observed under CLSM at various time points. As shown in Figure 7A, AA-NLC-TF showed significantly stronger blue fluorescence signals compared to the NLC-TF at all time points. The blue fluorescence was intensified in the cancerous cell after 4 h in the AA-NLC-TF group compared to the nontargeted NLC-TF-treated group, and the fluorescence was further intensified as time prolonged to 12 h. The difference in the intensities emphasized that the enhanced accumulation of AA-NLC-TF nanoparticles was mediated by the binding of AA conjugated nanocarriers to the sigma receptors (receptor-mediated
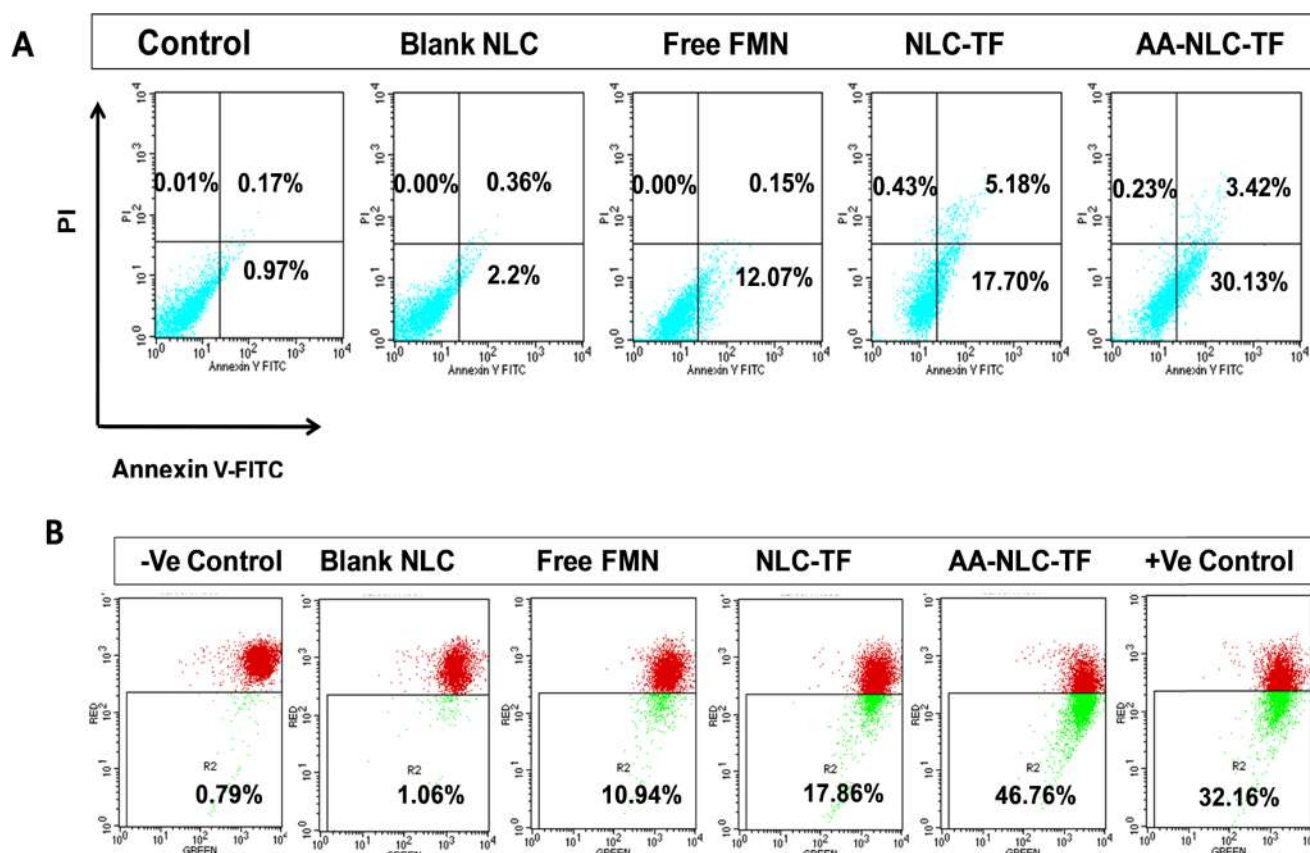
**Figure 9.** A) Dot plots representing the level of apoptosis in MDA-MB 231 cells after treatment with blank NLC, free FMN, NLC-TF, and AA-NLC-TF for 48 h. (B) Mitochondrial membrane potential of MDA-MB 231 cells generated after treatment with blank NLC, free FMN, NLC-TF, and AA-NLC-TF for 24 h. PBS-treated cells served as negative control, whereas FCCP-treated cells served as positive control.

uptake), whereas NLC-TF did not participate in receptor-mediated uptake, leading to lower fluorescence intensity in the MDA-MB 231 cell lines. For further confirmation of the intracellular trafficking of both the AA-NLC-TF and NLC-TF nanocarriers in the cancer cells, flow cytometric analysis (Figure 7B) was carried out as it analyzes the larger population of cells, and corroborative results were obtained with those of CLSM. As shown in Figure 7C, the higher mean fluorescence intensity of AA-NLC-TF showed that the uptake of AA-NLC-TF was higher than that of NLC-TF. To demonstrate the involvement of sigma receptors during endocytosis and to ensure this phenomenon, MDA-MB 231 cells were preincubated with 100 $\mu$M free AA to saturate the receptors, followed by addition of both unmodified (NLC-TF) and surface-modified NLCs (AA-NLC-TF). After 6 h, we observed that the mean fluorescence intensity was similar in both types of formulations (Figure 7D). This analysis demonstrates the evidence of binding of AA to sigma receptors as well as the role of sigma receptors in enhancing the cellular uptake as well as the prospect of using this sigma receptor binding ligand for the diagnosis and targeted therapy for breast cancer.

Next, the uptake studies were also performed on 4T1 breast cancer cells (Figure S2). Similar to the results of MDA-MB 231 cells, the higher fluorescence intensity was observed under CLSM in AA-NLC-TF-treated group in comparison to NLC-TF. Results further confirmed by the flow cytometer also indicated the higher accumulation of AA-NLC-TF nanoparticles than the nontargeted nanoparticles.

**3.10. Cell Cycle Arrest in MDA-MB 231 Cells.** FMN induces the cell cycle arrest at G2/M phase in MDA-MB 231 cell lines via PI3K−Akt signaling pathway and triggers apoptosis in vitro and in vivo.[45] Figure 8 comprises the effect of free FMN and FMN-loaded NLC formulations along with blank NPs on MDA-MB 231 cell cycle for various time intervals. After 24 h, free FMN, NLC-TF, and AA-NLC-TF arrested the cells in G2/M phase compared to the control. Moreover, this percentage of cells in G2/M phase gradually increased in 48 h upon treatment with the above formulations. AA-NLC-TF (58.06%) showed much higher cell cycle arrest compared to free drug (12.96%) and NLC-TF (38.67%), which demonstrated the enhanced anticancer potential of targeted nanoparticles in cancer cells.

**3.11. FMN-Loaded Targeted NLC NPs Enhance Apoptosis in MDA-MB 231 Cells.** Despite apoptosis being the cause of various problems, it plays a vital role in the treatment of cancer as it is a popular target for various chemotherapy regimens. To investigate the effect of free FMN and FMN containing nanoparticles, quantitative evaluation of their apoptotic potential was done using flow cytometry with the aid of dual staining agents (PI and Annexin V−FITC). As shown in Figure 9A, the lower right quadrants of the dot plots represent the early apoptotic cells, whereas the upper right and upper left quadrants show the late apoptotic and necrotic cells, respectively. Results showed that the apoptotic effect of AA-NLC-TF was more pronounced than free FMN treatment. The apoptotic effect of AA-NLC-TF (33.55%) enhanced in comparison to NLC-TF (22.88%), free FMN (12.22%), and
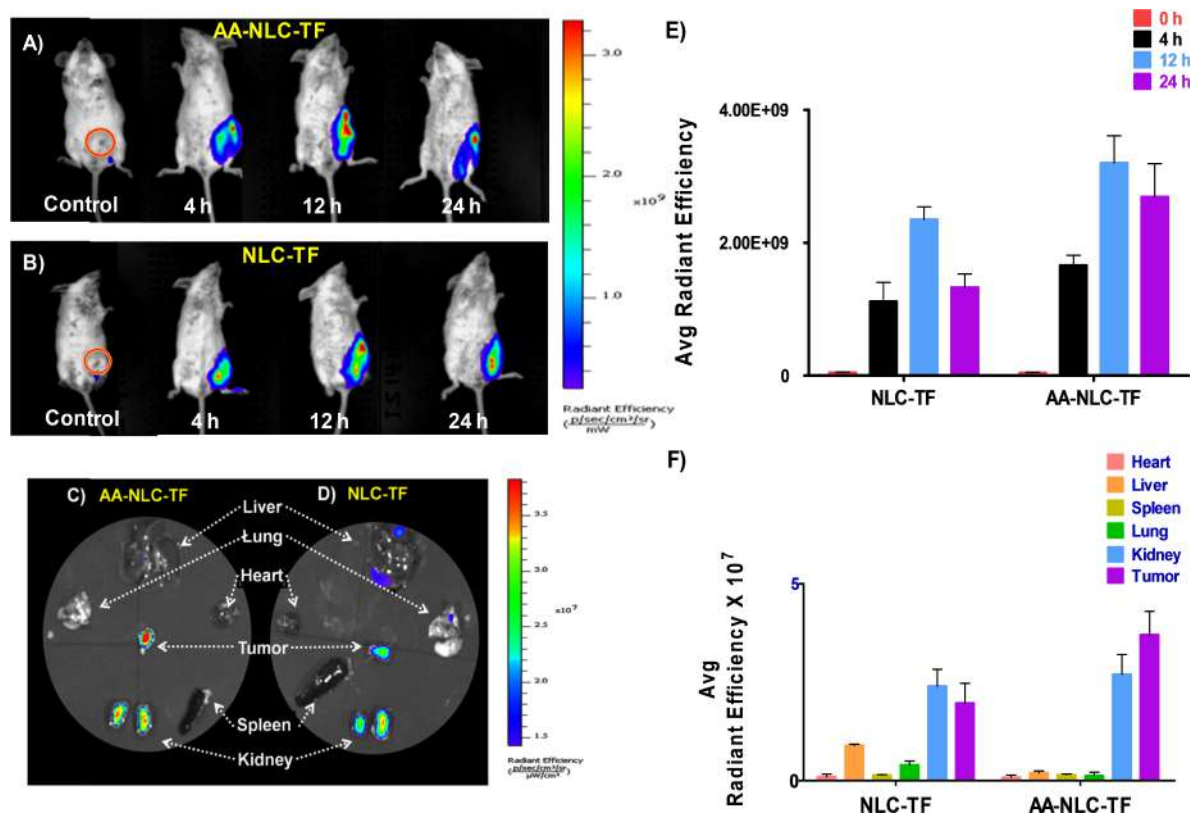
**Figure 10.** In vivo tumor imaging and tumor-targeting study after iv injection of NLC formulation. (A, B) Body imaging of targeted group and nontargeted group; tumor locations were marked by red circles. (C, D) Ex vivo imaging of major organs from 4T1 tumor-bearing mice at 12 h post injection of the above-mentioned group. (E) In vivo quantification of tumor-associated fluorescence signals of TPE-loaded NLC NPs. (F) Ex vivo quantification of fluorescence signals of TPE-loaded NLC NPs in other major organs. All data are shown as mean $\pm$ SD ($n$ = 3).

blank NLC (2.56%). As stated previously, sigma receptors played a vital role in the uptake of AA-NLC-TF. Reduced apoptotic effects observed after treatment with NLC-TF may be due to its nontargeting property, and the findings summarized in Figure 9A demonstrate the apoptotic effect of treatment regimens and free drug.

**3.12. ROS Studies.** The DCFH-DA assay quantitatively detects the intracellular production of ROS species like superoxide and hydrogen peroxide. Usually, mitochondrial ROS production occurs as natural products during metabolic processes, but their level increases in response to stress, which leads to damage to plasma membrane, DNA, and cellular damage. Eventually, it initiates the intrinsic apoptosis pathway of the cell. In this experiment, after treatment with both the types of NLC NPs and with free drug, the significant and increased production of ROS levels was detected. DCFH-DA, a permeant probe, was taken up by the attached cells and converted into fluorescent dichlorofluorescein (DCF) product, whose fluorescence intensity was measured using a flow cytometer. Results showed that AA-NLC-TF significantly increased the ROS level ($P < 0.001$) compared to NLC-TF and free FMN in 12 and 24 h, which indicated the negative impact of targeted nanoparticles on cellular viability. The mean fluorescence intensities of free FMN, NLC-TF, and AA-NLC-TF are shown in Figure S4.

**3.13. In Vivo Optical Imaging.** After superior in vitro activity, TPE- and FMN-loaded NLC NPs were examined for in vivo bioimaging applications. 4T1 metastatic breast cancer mice model, which was established by the subcutaneous injection of 4T1 cells into the BALB/c mice, was used as the

animal model. After intravenous injection of TPE-bearing nanoparticles (dose, 1 mg/kg TPE equivalent), the mice were imagined using IVIS Kinetic Imaging System (Caliper Life Sciences).

Figure 10A,B shows the time-dependent tumor accumulation of TPE-loaded nanoparticles in 4T1-cell-induced tumor-bearing mice. A high intense fluorescence was observed after 12 h post injection of AA-NLC-TF compared to the NLC-TF-treated group, indicating a higher localization of targeted nanoparticles (AA-NLC-TF) in the tumor tissue. The capability of the TPE-loaded AA-NLC-TF nanoparticles to illuminate the tumor tissue selectively with high contrast may be associated with dual factors. The first factor is the intense fluorescence of AIE fluorogen-TPE accumulated in the tumor, whereas the second factor includes active tumor-targeting ability of the nanoparticles by the AA ligand. In case of NLC-TF-treated animals, we observed relatively bright fluorescence at 12 h post injection, but it had diminished after 24 h. This relatively weak fluorescence of NLC-TF at tumor site was attributed to its nontargetability and consecutive low accumulation of NLC-TF NPs. Interestingly, the fluorescence signal of AA-NLC-TF persisted even after 24 h of injection, and its higher fluorescence intensity compared to NLC-TF, as shown in Figure 10E, clearly indicate that the TPE-encapsulated AA-NLC-TF nanoparticles can be used as an effective optical beacon for in vivo tumor diagnosis with high specificity and good fluorescence contrast.

The prominent active targeting of nanoparticles was also demonstrated using the ex vivo fluorescence imaging of excised tumor tissues and other major organs. As shown in Figure
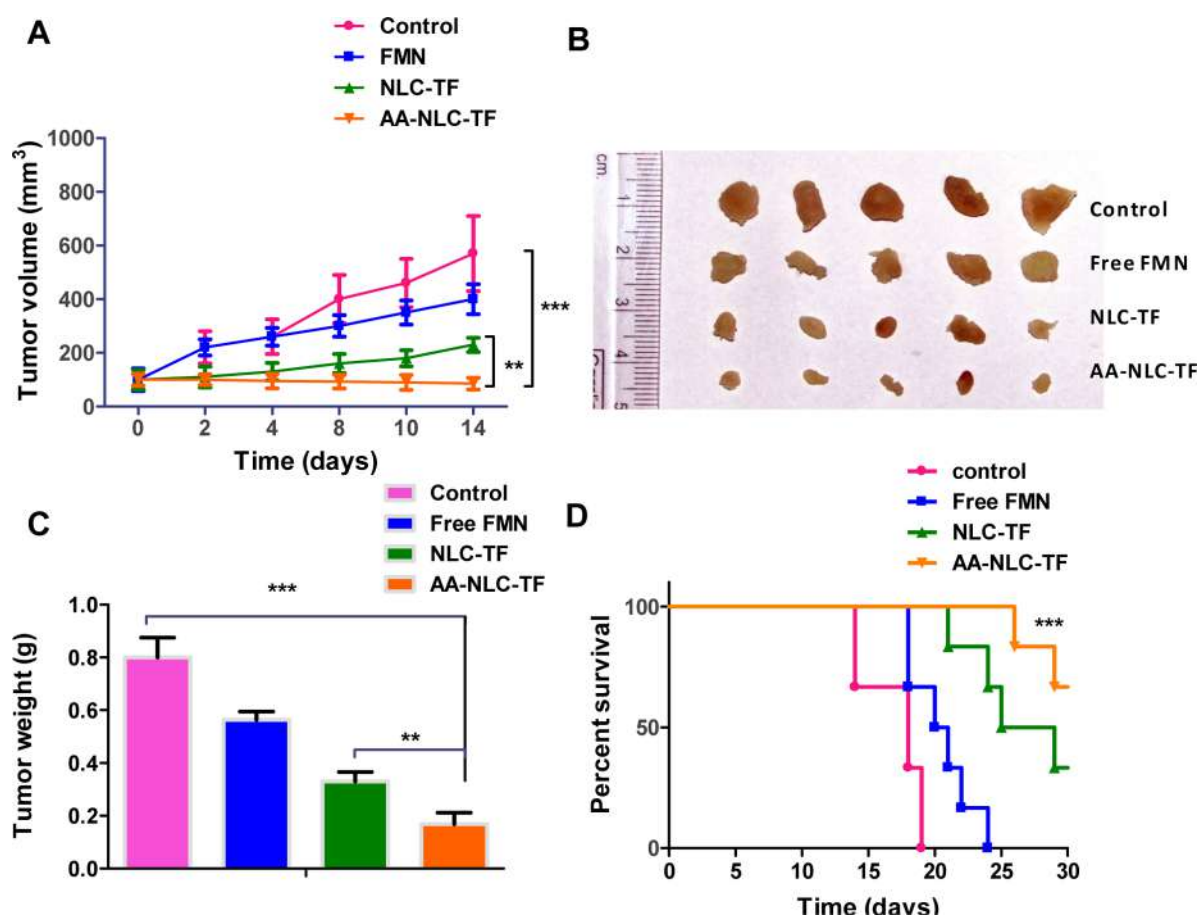
**Figure 11.** In vivo antitumor activity against 4T1 cells transplanted mammary tumor in BALB/c (FMN dose: 10 mg/kg body weight). (A) Tumor volume vs time at different time points of the study ($n = 6$). (B) Morphology of the tumors harvested at the end of the study. (C) Weights of the tumors excised at the end of the tumor regression study. (D) Survival rates of 4T1 tumor-bearing mice administrated with free FMN, NLC-TF, AA-NLC-TF, and PBS (control) ($n = 6$). (In tumor regression and survival studies, "day 0" represents the day when tumor volume reached ∼100 mm³ after the inoculation of cells and the treatment started; ***$P < 0.001$ represents control vs AA-NLC-TF, and **$P < 0.05$ represents NLC-TF vs AA-NLC-TF.)

10C,D the difference in the fluorescence intensity between groups treated with nontargeted and targeted nanoparticles was due to the differential distribution of nanoparticles. Bright red emission (Figure 10C) and higher fluorescence intensity (Figure 10F) of targeted nanoparticles (AA-NLC-TF) in the tumor than other organs were due to active tumor-targeting ability of the nanoparticles bearing AA ligand. However, relatively weak fluorescence of NLC-TF nanoparticles at the tumor site and high fluorescence in other major organs were attributed to their nontargetability and systemic distribution. This demonstrated the specific targeting ability of AA-NLC-TF to the tumor that contains sigma receptor-overexpressed cancer cells in a living body.

**3.14. In Vivo Antitumor Efficacy.** Benefiting from the cancer cell-specific internalization, 4T1 breast carcinoma-bearing mice were used to evaluate the antitumor efficacy of AA-NLC-TF NPs in vivo compared to NLC-TF, free FMN, and control. The 4T1 cells closely resemble human-derived metastatic breast cancer cell line MDA-M 231. Both the cell lines are estrogen-independent breast cancer cell lines and express sigma receptors and therefore 4T1 cells could be used as a suitable in vivo model for the evaluation of anticancer efficacy of NLC formulations.[46] Treatment was started when the tumor volume reached 100 mm³ in all of the animals. Each group received iv dose of 10 mg/kg FMN equivalent every 2

days for seven times. As shown in the tumor volume curve in Figure 11A and tumor photographs in Figure 11B, the tumor volume of the control group treated with blank NLC NPs increased significantly, whereas that of the AA-NLC-TF-treated tumors showed almost no growth. The average tumor volume of the free FMN-treated groups was smaller than that of the control group, and the tumor volume of the AA-NLC-TF group was significantly smaller than that of both the NLC-TF-treated group ($P < 0.001$) and the control group ($P < 0.05$). At the end of the tumor regression study, tumors were excised and the average weight of the tumors was assessed (Figure 11C); the tumor inhibition rates of free FMN-, NLC-TF-, and AA-NLC-TF-treated groups were 29.50, 58.75, and 79.00% respectively. The tumor weight of the AA-NLC-TF-treated group at the end of the tumor regression study was 4.76-fold lower than the control group and 3.35-fold lower than the free FMN group. The results indicated that the active targeting of FMN in NLC NPs form improved its anticancer efficacy compared to the free form of FMN. For evaluating the safety of the formulation, body weight of all of the treated groups was determined. Compared to the control mice, weights of the NLC formulations and free FMN-treated mice remained almost unchanged, which indicate the in vivo biocompatibility of the NLC NPs and use of this nanoparticles as a safe bioagent.

**3.15. Survival Analysis.** The Kaplan–Meier survival plot in Figure 11D showed the median survival rate of all of the treated groups. Survival studies were performed for 30 days after the treatment of mice. The median survival of NLC-TF was 27 days significantly longer than the control group (median survival, 18 days) and free FMN-treated mice (median survival, 21 days). Treatment with FMN increased the survival time of the mice by 3 days compared to control. However, the median survival rate of targeted AA-NLC-TF NPs prolonged the survival of mice (median survival, >30 days), which indicated the improved efficacy of FMN by the targeted delivery system.

## 4. CONCLUSIONS

Sigma receptor-targeted AA-NLC-TF combines a unique AIE effect with the controlled release of the chemotherapeutic agent FMN. To the best of our knowledge, this is the first report of liquid crystalline phase particles loaded with FMN for the treatment of breast cancer. This theranostic approach not only reports the location of the tumor by AIE effects, but also facilitates intracellular drug release following receptor-mediated endocytosis for optimized therapeutic effect. Furthermore, strategic use of high lipid volume fractioned liquid crystalline particles circumvent the poor solubility issue of FMN, which results in high loading. Our results demonstrated the specific binding of AA-NLC-TF to sigma receptor positive MDA-MB 231 and 4T1 cells, and systemic delivery of AA-NLC-TF significantly inhibited tumor growth in a 4T1-induced breast cancer xenograft model. Moreover, we showed that targeted delivery of AA-NLC-TF and the presence of tumor could be detected noninvasively by the active AIE imaging in comparison to nontargeted NLC-TF nanoparticles. Conclusively, aggregation-induced emission fluorogen-based nano-theranostics developed in this study could be a promising platform for imaging and targeted noninvasive oncotherapy.

## ■ ASSOCIATED CONTENT

### Ⓢ Supporting Information

The Supporting Information is available free of charge on the ACS Publications website at DOI: 10.1021/acsami.7b19109.

> Synthesis of Pluronic F127–anisamide conjugate (PF127-AA), quantification of FMN and TPE by HPLC method, hemolysis assay, cytotoxicity of blank and AA-NLC-TF NPs particles on J774.2 cells, uptake of NLC NPs in 4T1 cells after treatment for 12 h, and ROS activity in MDA-MB 231 after treatment with free FMN, NLC-TF, and AA-NLC-TF for 12 and 24 h (PDF)

## ■ AUTHOR INFORMATION

### Corresponding Author

*E-mail: prabhat_mishra@cdri.res.in, mishrapr@hotmail.com. Phone: +91-522-2612411(4537). Fax: +91-522-2623405.

### ORCID Ⓘ

Sandeep Urandur: 0000-0001-5803-077X
Pratibha Ramarao: 0000-0001-6666-5417
Prabhat Ranjan Mishra: 0000-0002-7418-8283

### Notes

The authors declare no competing financial interest.
CDRI communication number for this manuscript is 9667.

## ■ REFERENCES

(1) Kerlikowske, K.; Zhu, W.; Tosteson, A. N. A.; et al. Identifying women with dense breasts at high risk for interval cancer: A cohort study. *Ann. Intern. Med.* **2015**, *162*, 673–681.

(2) Oeffinger, K. C.; Fontham, E. T. H.; Etzioni, R.; et al. Breast cancer screening for women at average risk: 2015 guideline update from the American Cancer Society. *J. Am. Med. Assoc.* **2015**, *314*, 1599–1614.

(3) Scheel, J. R.; Lee, J. M.; Sprague, B. L.; Lee, C. I.; Lehman, C. D. Screening Ultrasound as an Adjunct to Mammography in Women with Mammographically Dense Breasts. *Am. J. Obstet. Gynecol.* **2015**, *212*, 9–17.

(4) Wu, T.-J.; Tzeng, Y.-K.; Chang, W.-W.; Cheng, C.-A.; Kuo, Y.; Chien, C.-H.; Chang, H.-C.; Yu, J. Tracking the engraftment and regenerative capabilities of transplanted lung stem cells using fluorescent nanodiamonds. *Nat. Nanotechnol.* **2013**, *8*, 682–689.

(5) Gao, X.; Cui, Y.; Levenson, R. M.; Chung, L. W. K.; Nie, S. In vivo cancer targeting and imaging with semiconductor quantum dots. *Nat. Biotechnol.* **2004**, *22*, 969.

(6) Oh, E.; Liu, R.; Nel, A.; Gemill, K. B.; Bilal, M.; Cohen, Y.; Medintz, I. L. Meta-analysis of cellular toxicity for cadmium-containing quantum dots. *Nat. Nanotechnol.* **2016**, *11*, 479–486.

(7) Wang, D.; Qian, J.; He, S.; Park, J. S.; Lee, K.-S.; Han, S.; Mu, Y. Aggregation-enhanced fluorescence in PEGylated phospholipid nano-micelles for in vivo imaging. *Biomaterials* **2011**, *32*, 5880–5888.

(8) Han, X.; Liu, D.-E.; Wang, T.; Lu, H.; Ma, J.; Chen, Q.; Gao, H. Aggregation-Induced-Emissive Molecule Incorporated into Polymeric Nanoparticulate as FRET Donor for Observing Doxorubicin Delivery. *ACS Appl. Mater. Interfaces* **2015**, *7*, 23760–23766.

(9) Caltagirone, C.; Arca, M.; Falchi, A. M.; Lippolis, V.; Meli, V.; Monduzzi, M.; Nylander, T.; Rosa, A.; Schmidt, J.; Talmon, Y.; Murgia, S. Solvatochromic fluorescent BODIPY derivative as imaging agent in camptothecin loaded hexosomes for possible theranostic applications. *RSC Adv.* **2015**, *5*, 23443–23449.

(10) Meli, V.; Caltagirone, C.; Sinico, C.; Lai, F.; Falchi, A. M.; Monduzzi, M.; Obiols-Rabasa, M.; Picci, G.; Rosa, A.; Schmidt, J.; et al. Theranostic hexosomes for cancer treatments: an in vitro study. *New J. Chem.* **2017**, *41*, 1558–1565.

(11) Nilsson, C.; Barrios-Lopez, B.; Kallinen, A.; Laurinmäki, P.; Butcher, S. J.; Raki, M.; Weisell, J.; Bergström, K.; Larsen, S. W.; Østergaard, J.; et al. SPECT/CT imaging of radiolabeled cubosomes and hexosomes for potential theranostic applications. *Biomaterials* **2013**, *34*, 8491–8503.

(12) Szlezak, M.; Nieciecka, D.; Joniec, A.; Pękała, M.; Gorecka, E.; Emo, M.; Stébé, M. J.; Krysiński, P.; Bilewicz, R. Monoolein Cubic Phase Gels and Cubosomes Doped with Magnetic Nanoparticles−Hybrid Materials for Controlled Drug Release. *ACS Appl. Mater. Interfaces* **2017**, *9*, 2796–2805.

(13) Rodrigues, L.; Kyriakos, K.; Schneider, F.; Dietz, H.; Winter, G.; Papadakis, C. M.; Hubert, M. Characterization of lipid-based hexosomes as versatile vaccine carriers. *Mol. Pharmaceutics* **2016**, *13*, 3945–3954.

(14) Suga, K.; Kondo, D.; Otsuka, Y.; Okamoto, Y.; Umakoshi, H. Characterization of aqueous oleic acid/oleate dispersions by fluorescent probes and Raman spectroscopy. *Langmuir* **2016**, *32*, 7606−7612.

(15) Zhu, Z.; Qian, J.; Zhao, X.; Qin, W.; Hu, R.; Zhang, H.; Li, D.; Xu, Z.; Tang, B. Z.; He, S. Stable and Size-Tunable Aggregation-Induced Emission Nanoparticles Encapsulated with Nanographene Oxide and Applications in Three-Photon Fluorescence Bioimaging. *ACS Nano* **2016**, *10*, 588−597.

(16) Han, K.; Wang, S.-B.; Lei, Q.; Zhu, J.-Y.; Zhang, X.-Z. Ratiometric Biosensor for Aggregation-Induced Emission-Guided Precise Photodynamic Therapy. *ACS Nano* **2015**, *9*, 10268−10277.

(17) Mei, J.; Leung, N. L. C.; Kwok, R. T. K.; Lam, J. W. Y.; Tang, B. Z. Aggregation-Induced Emission: Together We Shine, United We Soar! *Chem. Rev.* **2015**, *115*, 11718−11940.

(18) Liu, J.; Chen, C.; Ji, S.; Liu, Q.; Ding, D.; Zhao, D.; Liu, B. Long wavelength excitable near-infrared fluorescent nanoparticles with aggregation-induced emission characteristics for image-guided tumor resection. *Chem. Sci.* **2017**, *8*, 2782−2789.

(19) RamaKrishna, N. V. S.; Devanesan, P. D.; Rogan, E. G.; Cavalieri, E. L.; Jeong, H.; Jankowiak, R.; Small, G. J. Mechanism of metabolic activation of the potent carcinogen 7,12-dimethylbenz[a]-anthracene. *Chem. Res. Toxicol.* **1992**, *5*, 220−226.

(20) Xu, G.; Lin, G.; Lin, S.; Wu, N.; Deng, Y.; Feng, G.; Chen, Q.; Qu, J.; Chen, D.; Chen, S.; et al. The Reproductive Toxicity of CdSe/ZnS Quantum Dots on the in vivo Ovarian Function and in vitro Fertilization. *Sci. Rep.* **2016**, *6*, No. 37677.

(21) Aldred, M. P.; Li, C.; Zhu, M.-Q. Optical Properties and Photo-Oxidation of Tetraphenylethene-Based Fluorophores. *Chem. − Eur. J.* **2012**, *18*, 16037−16045.

(22) Zhu, Z.; Song, B.; Yuan, J.; Yang, C. Enabling the Triplet of Tetraphenylethene to Sensitize the Excited State of Europium(III) for Protein Detection and Time-Resolved Luminescence Imaging. *Adv. Sci.* **2016**, *3*, No. 1600146.

(23) Yu, G.; Cook, T. R.; Li, Y.; Yan, X.; Wu, D.; Shao, L.; Shen, J.; Tang, G.; Huang, F.; Chen, X.; Stang, P. J. Tetraphenylethene-based highly emissive metallacage as a component of theranostic supra-molecular nanoparticles. *Proc. Natl. Acad. Sci. U.S.A.* **2016**, *113*, 13720−13725.

(24) Dasargyri, A.; Hervella, P.; Christiansen, A.; Proulx, S. T.; Detmar, M.; Leroux, J.-C. Findings questioning the involvement of Sigma-1 receptor in the uptake of anisamide-decorated particles. *J. Controlled Release* **2016**, *224*, 229−238.

(25) Aydar, E.; Onganer, P.; Perrett, R.; Djamgoz, M. B.; Palmer, C. P. The expression and functional characterization of sigma (σ) 1 receptors in breast cancer cell lines. *Cancer Lett.* **2006**, *242*, 245−257.

(26) Ramya, A. N.; Joseph, M. M.; Nair, J. B.; Karunakaran, V.; Narayanan, N.; Maiti, K. K. New insight of tetraphenylethylene-based Raman signatures for targeted SERS nanoprobe construction toward prostate cancer cell detection. *ACS Appl. Mater. Interfaces* **2016**, *8*, 10220−10225.

(27) Zhang, S.; Tang, X.; Tian, J.; Li, C.; Zhang, G.; Jiang, W.; Zhang, Z. Cardioprotective effect of sulphonated formononetin on acute myocardial infarction in rats. *Basic Clin. Pharmacol. Toxicol.* **2011**, *108*, 390−395.

(28) Gautam, J.; Khedgikar, V.; Kushwaha, P.; Choudhary, D.; Nagar, G. K.; Dev, K.; Dixit, P.; Singh, D.; Maurya, R.; Trivedi, R. Formononetin, an isoflavone, activates AMP-activated protein kinase/β-catenin signalling to inhibit adipogenesis and rescues C57BL/6 mice from high-fat diet-induced obesity and bone loss. *Br. J. Nutr.* **2017**, *117*, 645−661.

(29) Vitale, D. C.; Piazza, C.; Melilli, B.; Drago, F.; Salomone, S. Isoflavones: estrogenic activity, biological effect and bioavailability. *Eur. J. Drug Metab. Pharmacokinet.* **2013**, *38*, 15−25.

(30) Singh, S. P.; Wahajuddin, M.; Tewari, D.; Pradhan, T.; Jain, G. K. PAMPA permeability, plasma protein binding, blood partition, pharmacokinetics and metabolism of formononetin, a methoxylated isoflavone. *Food Chem. Toxicol.* **2011**, *49*, 1056−1062.

(31) Tolleson, W. H.; Doerge, D. R.; Churchwell, M. I.; Marques, M. M.; Roberts, D. W. Metabolism of biochanin A and formononetin by human liver microsomes in vitro. *J. Agric. Food Chem.* **2002**, *50*, 4783−4790.

(32) Wang, X.; Yang, Y.; Zhuang, Y.; Gao, P.; Yang, F.; Shen, H.; Guo, H.; Wu, D. Fabrication of pH-responsive nanoparticles with an AIE feature for imaging intracellular drug delivery. *Biomacromolecules* **2016**, *17*, 2920−2929.

(33) Garti, N. *Self-Assembled Supramolecular Architectures: Lyotropic Liquid Crystals*; John Wiley & Sons, 2012; Vol. 3.

(34) Muller, F.; Salonen, A.; Glatter, O. Phase behavior of Phytantriol/water bicontinuous cubic Pn3m cubosomes stabilized by Laponite disc-like particles. *J. Colloid Interface Sci.* **2010**, *342*, 392−398.

(35) Sharma, S.; Verma, A.; Singh, J.; Teja, B. V.; Mittapelly, N.; Pandey, G.; Urandur, S.; Shukla, R. P.; Konwar, R.; Mishra, P. R. Vitamin B6 Tethered Endosomal pH Responsive Lipid Nanoparticles for Triggered Intracellular Release of Doxorubicin. *ACS Appl. Mater. Interfaces* **2016**, *8*, 30407−30421.

(36) Verma, A.; Sharma, S.; Gupta, P. K.; Singh, A.; Teja, B. V.; Dwivedi, P.; Gupta, G. K.; Trivedi, R.; Mishra, P. R. Vitamin B12 functionalized layer by layer calcium phosphate nanoparticles: A mucoadhesive and pH responsive carrier for improved oral delivery of insulin. *Acta Biomater.* **2016**, *31*, 288−300.

(37) Dian, L.; Yang, Z.; Li, F.; Wang, Z.; Pan, X.; Peng, X.; Huang, X.; Guo, Z.; Quan, G.; Shi, X.; Chen, B.; Li, G.; Wu, C. Cubic phase nanoparticles for sustained release of ibuprofen: formulation, characterization, and enhanced bioavailability study. *Int. J. Nanomed.* **2013**, *8*, 845−854.

(38) Nasr, M.; Dawoud, M. Sorbitol based powder precursor of cubosomes as an oral delivery system for improved bioavailability of poorly water soluble drugs. *J. Drug Delivery Sci. Technol.* **2016**, *35*, 106−113.

(39) Thapa, R. K.; Choi, J. Y.; Poudel, B. K.; Hiep, T. T.; Pathak, S.; Gupta, B.; Choi, H.-G.; Yong, C. S.; Kim, J. O. Multilayer-coated liquid crystalline nanoparticles for effective sorafenib delivery to hepatocel-lular carcinoma. *ACS Appl. Mater. Interfaces* **2015**, *7*, 20360−20368.

(40) Sharma, S.; Singh, J.; Verma, A.; Teja, B. V.; Shukla, R. P.; Singh, S. K.; Sharma, V.; Konwar, R.; Mishra, P. Hyaluronic acid anchored paclitaxel nanocrystals improves chemotherapeutic efficacy and inhibits lung metastasis in tumor-bearing rat model. *RSC Adv.* **2016**, *6*, 73083−73095.

(41) Ma, X.; Tao, H.; Yang, K.; Feng, L.; Cheng, L.; Shi, X.; Li, Y.; Guo, L.; Liu, Z. A functionalized graphene oxide−iron oxide nanocomposite for magnetically targeted drug delivery, photothermal therapy, and magnetic resonance imaging. *Nano Res.* **2012**, *5*, 199−212.

(42) Driever, C. D.; Mulet, X.; Waddington, L. J.; Postma, A.; Thissen, H.; Caruso, F.; Drummond, C. J. Layer-by-layer polymer coating on discrete particles of cubic lyotropic liquid crystalline dispersions (cubosomes). *Langmuir* **2013**, *29*, 12891−12900.

(43) Boyd, B. J.; Rizwan, S. B.; Dong, Y.-D.; Hook, S.; Rades, T. Self-Assembled Geometric Liquid-Crystalline Nanoparticles Imaged in Three Dimensions: Hexosomes Are Not Necessarily Flat Hexagonal Prisms. *Langmuir* **2007**, *23*, 12461−12464.

(44) Rizwan, S. B.; Dong, Y. D.; Boyd, B. J.; Rades, T.; Hook, S. Characterisation of bicontinuous cubic liquid crystalline systems of phytantriol and water using cryo field emission scanning electron microscopy (cryo FESEM). *Micron* **2007**, *38*, 478−485.

(45) Wu, X. Y.; Xu, H.; Wu, Z. F.; Chen, C.; Liu, J. Y.; Wu, G. N.; Yao, X. Q.; Liu, F. K.; Li, G.; Shen, L. Formononetin, a novel FGFR2 inhibitor, potently inhibits angiogenesis and tumor growth in preclinical models. *Oncotarget* **2015**, *6*, 44563.

(46) Ma, G.; He, J.; Yu, Y.; Xu, Y.; Yu, X.; Martinez, J.; Lonard, D. M.; Xu, J. Tamoxifen Inhibits ER-negative Breast Cancer Cell Invasion and Metastasis by Accelerating Twist1 Degradation. *Int. J. Biol. Sci.* **2015**, *11*, 618−628.